

Probing Large Scale Ionizing Background Fluctuation with Lyman α Forest and Galaxy Cross-correlation at $z=2.4$

Heyang Long^{1,2*} and Christopher M. Hirata^{1,2,3†}

¹Department of Physics, The Ohio State University, 191 West Woodruff Avenue, Columbus, Ohio 43210, USA

²Center for Cosmology and AstroParticle Physics (CCAPP), The Ohio State University, 191 West Woodruff Avenue, Columbus, Ohio 43210, USA

³Department of Astronomy, The Ohio State University, 140 West 18th Avenue, Columbus, Ohio 43210, USA

19 January 2023

ABSTRACT

The amplitude of the metagalactic ultraviolet background (UVB) at large-scales is impacted by two factors. First, it naturally attenuates at scales larger than mean-free-path of UVB photons due to the absorption by neutral intergalactic medium. Second, there are discrete and rare ionizing sources distributing in the Universe, emitting the UVB photons, and thus enhancing the local UVB amplitude. Therefore, for cosmological probe that is sensitive to the UVB amplitude and capable of detecting the large scale like Lyman- α forest spectrum, the fluctuation due to the clustering of ionizing sources becomes a significant factor for Lyman- α flux transmission and leave imprints on Lyman- α flux power spectrum at these large scales. In this work, we make use of a radiative transfer model that parametrizes the UVB source distribution by its bias b_j and shot noise \bar{n}_j . We estimate the constraints on this model through the cross-correlation between Lyman- α forest survey and galaxy survey, using the DESI Lyman- α forest survey and the Roman Space Telescope emission line galaxy survey as an example. We show the detection sensitivity improvement for UVB parameters from disjoint to maximal overlap of DESI+Roman survey strategy. We also show that the degeneracy of two ionizing source parameters can be broken by increasing the overlapping survey area. Our results motivate survey strategies more dedicated to probe the UVB large-scale fluctuations.

Key words: intergalactic medium - cosmology: large-scale structure of Universe

1 INTRODUCTION

The intergalactic medium (IGM) after the Epoch of Reionization (EoR) is maintained highly ionized by metagalactic ultraviolet background (UVB), which is generated by star-forming galaxies (SFGs) and quasars (see Robertson 2022; Wise 2019; Puchwein et al. 2019; McQuinn 2016 for a review). Determining the amplitude and spectral shape of UVB as a function of redshift is critical to understand relative contributions from ionizing sources (Faucher-Giguère et al. 2008). Moreover, in practice the post-reionization thermal and ionization state of intergalactic medium (IGM) and structure formation is usually simulated in light of a spatially uniform UVB.

There are various ways to measure UVB through cosmic epoch. The proximity effect has been a classical probe of UVB intensity for years (Bajtlik et al. 1988; Carswell et al. 1987; Dall’Aglio & Gnedin 2010; Dall’Aglio et al. 2008; Calverley et al. 2011). Luminous quasars could produce large amounts of ionizing photons and thus enhance the transmission of the Lyman- α forest near themselves (up to several Mpc) (Becker et al. 2011).

While quasar luminosity determines the enhanced portion of transmission, the size of this “proximity zone” also depends on UVB intensity (e.g. Dall’Aglio et al. 2008; Calverley et al. 2011; Chen & Gnedin 2021). So with quasar luminosity known, the UVB intensity could be inversely deduced by comparing Lyman- α spectra in the proximity zone to those in the absence of quasar at the same redshift. An alternative way of estimating UVB intensity is developed by comparing simulated Lyman- α forest spectra to the real observation data (Bolton et al. 2005; Bolton & Haehnelt 2007; Becker & Bolton 2013; Khaire et al. 2019; Gallego et al. 2021). In numerical simulations the uniform UVB intensity can be adjusted to such that the mean transmitted flux \bar{F} of simulated Lyman- α forest spectra matches that of real observation data. However, there are degeneracies since the gas density distribution and IGM temperature also affect \bar{F} . The thermal evolution of the IGM, while not directly sensitive to the *amplitude* of the UVB, is sensitive to the spectral shape since this determines the mean photoionization heating per recombination (Hui & Gnedin 1997). A more direct way to estimate the UVB intensity is based on detections of individual sources, i.e SFGs (e.g. Steidel et al. 2018; Vanzella et al. 2012) and quasars (e.g. Cowie et al. 2009; Romano et al. 2019). Ionizing photons produced by massive stars or quasars could propagate beyond their local H II region, enlarging ionized bubbles and

* E-mail: long.1697@osu.edu

† E-mail: hirata.10@osu.edu

escaping unimpeded. By measuring the escaping fraction and mean free path (MFP) of the ionizing photons in addition to the source luminosity functions, the ionizing background intensity could be estimated.

The spatial fluctuations of IGM properties such as temperature (McQuinn et al. 2011; Keating et al. 2018) as well as UVB intensity (McDonald et al. 2005; White et al. 2010; Mesinger & Furlanetto 2009; D’Aloisio et al. 2018), could perturb the Lyman- α forest observable in corresponding scales. As implicated by the early work of Croft et al. (1999), the UVB fluctuation could have more important contribution to the fluctuation of Lyman- α forest power spectrum in the limit of very large scale. Previous works built analytical models to quantify the UVB fluctuation (Pontzen 2014; Suarez & Pontzen 2017; Gontcho A Gontcho et al. 2014; Meiksin & McQuinn 2019). Recent works show that it may affect the inferred bias of Ly α -emitting galaxies (Meiksin & Suarez 2022). Also, the effect on large scale structure could complicate the constraints on cosmological parameter such as neutrino mass m_ν , scalar spectral index n_s and non-Gaussianity f_{NL} in post-reionization large scale structure surveys (Upton Sanderbeck et al. 2019). Dedicated to measure the comoving $100 \text{ h}^{-1} \text{ Mpc}$ baryonic acoustic oscillation (BAO) feature in the correlation function, Baryonic Oscillation Spectroscopic Survey (BOSS; Dawson et al. 2013) has enabled the measurement of Lyman- α forest correlation function on large scales comparable to the mean free path of ionizing photons. As a successor of BOSS, the Dark Energy Spectroscopic Instrument (DESI; DESI Collaboration et al. 2016) will provide many more quasar sightlines and extend the redshift range with dense sampling, enhancing the viability of investigating astrophysical phenomena in large scales. Furthermore, sourced by discrete SFGs and quasars, the scale-dependent feature of UVB could shed light on the scale-dependent distribution of these source populations and how it traces the underlying matter distribution at large scale (Meiksin 2005).

In this work, we consider the scale-dependent ionizing background fluctuation in light of discrete source distribution at large scales, based on the modeling of this effect in Pontzen (2014). We take the UV source distribution into account in the biasing model and show its effect on the large scale feature of Lyman- α flux power spectrum and the cross-spectrum of the Lyman- α forest with a galaxy survey. The cross-correlation of multiple tracers can reduce cosmic variance since both the Lyman- α forest and the galaxies trace the same underlying structure (Seljak 2009; McDonald & Seljak 2009; Oxholm & Switzer 2021). Moreover, it breaks the degeneracy at large scales between the effective bias b_j and mean number density \bar{n}_j of ionizing sources (although not the degeneracy with the mean free path of ionizing photons; see Pontzen et al. 2014). We use the Fisher matrix framework to explore this in the context of a specific pair of surveys: the Lyman- α forest observations ongoing with DESI, and the [O III] emission line survey planned with the Nancy Roman Space Telescope (Spergel et al. 2015; Wang et al. 2022). We show that DESI-Roman cross-correlation could shed light on the origin of UVB photons and this power could be improved by increasing the overlapping survey volume of the two surveys.

This paper is structured as follows. In Section 2 we present our power spectrum expressions and Fisher matrix framework. In Section 3, we layout the realistic survey parameters and the choice of fiducial model parameter values priors implemented. The results are shown in Section 4 and conclusions are summarized in Section 5.

Throughout this work, we use cosmological parameters from the Planck 2015 “TT+TE+EE+lowP+lensing+ext” (Planck Collab-

oration et al. 2016): $\Omega_m = 0.3089$, $\Omega_\Lambda = 0.6911$, $\Omega_b h^2 = 0.02230$, $H_0 = 67.74 \text{ km s}^{-1} \text{ Mpc}^{-1}$, and $n_s = 0.9667$.

2 CROSS-CORRELATION OF LYMAN- α FOREST AND GALAXIES

2.1 Biasing Models

A cosmological biasing model quantifies how certain observables trace the fluctuation of matter density in the Universe as well as other physical effects by a factor of corresponding bias coefficients. For the Lyman- α forest the fluctuation of transmission flux is defined as

$$\delta_F = \frac{F}{\bar{F}(z)} - 1, \quad (1)$$

where F is the fraction of quasar flux transmission and $\bar{F}(z)$ is its mean as a function of redshift z .

The vanilla Lyman- α forest biasing model consider flux fluctuation at linear order with redshift space distortion effect:

$$\tilde{\delta}_F(\mathbf{k}) = b_F(1 + \beta_F \mu^2) \tilde{\delta}_m(\mathbf{k}), \quad (2)$$

where b_F is the usual Lyman- α flux bias, δ_m is the matter overdensity, β_F is the redshift distortion parameter and $\mu = \cos \theta = k_\parallel/k$ the angle between the Fourier wavevector and the line of sight. Since Lyman- α transmission is not conserved in the real-to-redshift space conversion, the usual relation (Kaiser 1987) $\beta = f/b$ (where f is the growth rate of structure and b is the bias) does not apply and β_F (or equivalently the biasing coefficient $b_\eta = b_F \beta_F / f \neq 1$) must be treated as a parameter. In this work, we would like to study the UVB source fluctuation by its imprints on Lyman- α flux power spectrum, particularly on its large scale feature. We adapt the H I biasing model built in Pontzen (2014) and summarize symbols throughout this work in Table 1. (Although the parametrization is somewhat different, the Gontcho A Gontcho et al. 2014 model includes a source bias and shot noise and has many of the same functional dependencies, and we expect that similar results could be obtained using that framework.) The H I overdensity in Fourier space in this model is written as

$$\tilde{\delta}_{\text{HI}}(\mathbf{k}) = b_{\text{HI}}(k) \tilde{\delta}_m(\mathbf{k}) - \frac{[1 - \beta_{\text{HI}} \beta_r] S(k)}{1 - \beta_{\text{HI}} S(k)} \tilde{\delta}_{\text{SN}}(\mathbf{k}). \quad (3)$$

The characteristic function $S(k)$ is the normalized Fourier transform of the flux profile from an ionizing source including both the inverse square law and exponential attenuation:

$$\begin{aligned} S(k) &= \int_{\mathbb{R}^3} a \kappa_{\text{tot}} e^{-a \kappa_{\text{tot}} r} \frac{1}{4\pi r^2} e^{i\mathbf{k}\cdot\mathbf{r}} d^3 r \\ &= \frac{a \kappa_{\text{tot}}}{k} \arctan \frac{k}{a \kappa_{\text{tot}}}, \end{aligned} \quad (4)$$

where the scale factor a converts from physical to comoving attenuation coefficient. The scale-dependent H I bias b_{HI} is

$$\begin{aligned} b_{\text{HI}}(k) &= \frac{b_{\text{HI,u}} - b_{j,\text{eff}} S(k)}{1 - \beta_{\text{HI}} S(k)} \\ &= \frac{b_{\text{HI,u}}}{1 - \beta_{\text{HI}} S(k)} \\ &\quad - \frac{[(1 - \beta_{\text{HI}} \beta_r) b_j - \beta_{\text{clump}} b_{\text{clump}} + \beta_{\text{HI}} \beta_r b_{\text{HI,u}}] S(k)}{1 - \beta_{\text{HI}} S(k)}, \end{aligned} \quad (5)$$

Table 1. Symbols used in this work.

Symbol	Definition
<i>Quantities included in Fisher matrix analysis as parameter</i>	
$b_{\text{HI,u}}$	Bias of H I in uniform UVB limit
b_{clump}	Bias of H I clumps
b_j	Effective bias of ionizing sources
$b_{F\delta}$	Bias of Lyman- α flux to matter overdensity
b_η	Bias of Lyman- α flux to peculiar velocity gradient
b_g	Bias of galaxy
β_r	Dimensionless recombination radiation
\bar{n}_j	Effective mean ionizing source number density
κ_{HI}	Physical Lyman-limit opacity from IGM H I and self-shielded clumps
p_{clump}	Fraction of self-shielded clumps opacity within κ_{HI} , $\kappa_{\text{clump}}/\kappa_{\text{HI}}$
<i>Other model quantities</i>	
b_{HI}	Scale-dependent H I bias
$b_{j,\text{eff}}$	Effective bias of sources including recombination
κ_{tot}	Effective total Lyman-limit opacity
β_{clump}	Fraction from self-shielded clumps opacity of total opacity, $\kappa_{\text{clump}}/\kappa_{\text{tot}}$
β_{HI}	Fraction from IGM opacity of total opacity, $\kappa_{\text{HI}}/\kappa_{\text{tot}}$
β_z	Fraction from effective redshifting opacity of total opacity
β_V	Fraction from effective volume dilution opacity of total opacity
$\tilde{\delta}_{\text{SN},j}$	Shot noise of source number density
$\tilde{\delta}_{\text{SN},g}$	Shot noise of galaxy number density
$\bar{n}_{\text{Ly}\alpha}$	Mean area number density of quasars in Lyman- α forest survey
\bar{n}_g	Effective mean galaxy number density

where we substitute the effective source bias $b_{j,\text{eff}}$ as given in Pontzen (2014):

$$b_{j,\text{eff}} = (1 - \beta_{\text{HI}}\beta_r)b_j - \beta_{\text{clump}}b_{\text{clump}} + \beta_{\text{HI}}\beta_r b_{\text{HI,u}}. \quad (6)$$

We incorporate the Lyman- α flux bias and redshift-space distortion into this H I model to get a Lyman- α flux biasing model. The Lyman- α flux fluctuation in Fourier space is written as

$$\begin{aligned} \tilde{\delta}_F(\mathbf{k}) &= \frac{b_{F\delta}}{b_{\text{HI,u}}} \tilde{\delta}_{\text{HI}}(\mathbf{k}) + b_\eta \mu^2 f \tilde{\delta}_m(\mathbf{k}) \\ &= \left[\frac{b_{\text{HI}}(k)b_{F\delta}}{b_{\text{HI,u}}} + b_\eta \mu^2 f \right] \tilde{\delta}_m(\mathbf{k}) \\ &\quad - \frac{b_{F\delta}}{b_{\text{HI,u}}} \frac{[1 - \beta_{\text{HI}}\beta_r]S(k)}{1 - \beta_{\text{HI}}S(k)} \tilde{\delta}_{\text{SN},j}. \end{aligned} \quad (7)$$

On small scales ($k \gg \kappa_{\text{tot}}$), $S(k)$ asymptotes to zero such that the model reduces to the uniform UVB background assumption since $b_{\text{HI}}(k) \rightarrow b_{\text{HI,u}}$. Conversely on large scales, $S(k \ll \kappa_{\text{tot}}) \rightarrow 1$, and so the bias becomes

$$\lim_{k \rightarrow 0} \frac{b_{\text{HI}}(k)b_{F\delta}}{b_{\text{HI,u}}} = \frac{1 - b_{j,\text{eff}}/b_{\text{HI,u}}}{1 - \beta_{\text{HI}}} b_{F\delta}. \quad (8)$$

If $b_{j,\text{eff}} > b_{\text{HI,u}}$, this can even flip sign and become positive – that is, ultra-large-scale overdensities can have increased rather than decreased transmitted flux F , because they have a more intense UVB. However with the scale cuts (k_{min}) we use in this paper, we usually do not enter this regime. Also in the case of ionizing background fluctuations, the shot noise term becomes important on large scales rather than small scales because of the scale dependence of $S(k)$. Another feature is that this bias diverges as $k \rightarrow 0$ if $\beta_{\text{HI}} = 1$ (see commentary in the introduction of Meiksin & McQuinn 2019). This is the limit where only diffuse intergalactic gas contributes to removal of ionizing photons, with the “clumpy” absorbers and redshifting turned off. The divergence occurs because in such a model, there are either enough recombinations in the IGM to produce the

H I required to absorb the ionizing photons contributed by sources (in which case the IGM recombinates) or not (in which case the UVB simply builds up with time, approaching ∞ in the time-steady limit due to Olbers’ paradox). A model with $\beta_{\text{HI}} = 1$ and finite UVB, balanced exactly on this phase transition, has an infinite coefficient for response to perturbations in the time-steady limit. In our fiducial model $\beta_{\text{HI}} = 0.59$; in general, in the presence of the clumping and redshifting “sinks” for UVB photons, the divergent bias problem does not apply.

For the galaxies, since we are interested mainly in the large scales, we take the simple linear biasing model

$$\tilde{\delta}_g(\mathbf{k}) = (b_g + f\mu^2)\tilde{\delta}_m(\mathbf{k}) + \tilde{\delta}_{\text{SN},g}(\mathbf{k}), \quad (9)$$

where f is the growth rate and $\tilde{\delta}_{\text{SN},g}$ is a galaxy shot noise term. Note that the “tracer” galaxy sample is not necessarily the same as the population of galaxies that is emitting the ionizing photons, so $b_{j,\text{eff}}$ and b_g are different parameters.

2.2 Power spectra

The auto-correlation power spectrum $P_F(k, \mu)$ of the Lyman- α flux transmission has three pieces: a biasing term coming from $\tilde{\delta}_m(\mathbf{k})$ that traces the matter power spectrum; an ionizing source shot noise term; and observational terms (themselves coming from the finite signal-to-noise ratio of quasar spectra, and the aliasing effect from sampling a finite density of sightlines). The first two can be derived

from Eq. (7).

$$\begin{aligned}
 P_F(k, \mu) = & \underbrace{b_F^2(k, \mu) P_m(k)}_{\text{biasing, } P_{F, \text{bHI}}} + \underbrace{\frac{1}{\bar{n}_j} \left[\frac{b_{F\delta}}{b_{\text{HI}, u}} \frac{(1 - \beta_{\text{HI}} \beta_r) S(k)}{1 - \beta_{\text{HI}} S(k)} \right]^2}_{\text{source shot noise, } P_{F, \text{SN}}^j} \\
 & + \underbrace{\frac{1}{\bar{n}_{\text{Ly}\alpha}} \left[P_F^{\text{noise}} + P_F^{\text{1D}} \right]}_{\text{observation noise, } P_{F, \text{SN}}^{\text{Ly}\alpha} + P_{F, \text{alias}}}, \quad (10)
 \end{aligned}$$

where P_m is the matter power spectrum calculated by CLASS (Blas et al. 2011). The effective flux bias b_F is given by

$$b_F(k, \mu) \equiv \frac{b_{\text{HI}}(k) b_{F\delta}}{b_{\text{HI}, u}} + b_\eta \mu^2 f. \quad (11)$$

The 1-dimensional noise power spectrum P_F^{noise} (McQuinn & White 2011) is

$$P_F^{\text{noise}} = [S/N]^{-2} \frac{\Delta \lambda_{\text{obs}}}{\lambda_{\text{Ly}\alpha}} \frac{c}{H(z)}, \quad (12)$$

where S/N is the signal noise in $\Delta \lambda_{\text{obs}} = 0.8 \text{ \AA}$ pixels, the rest-frame Lyman- α wavelength is $\lambda_{\text{Ly}\alpha} = 1216 \text{ \AA}$, c is the speed of light, and $H(z) = H_0 \sqrt{\Omega_m (1+z)^3 + \Omega_\Lambda}$. For the aliasing contribution P_F^{1D} we use the empirical function fitted with the BOSS dataset and likelihood method in Palanque-Delabrouille et al. (2013). Note that Karaçaylı et al. (2020) modifies the fitting function with a Lorentzian decay to better fit P_{1D} in the high- k regime ($k \sim 37 h \text{ Mpc}^{-1}$). But for k range considered in this work the high- k correction will not significantly impact the results, so for our purpose the empirical function in Palanque-Delabrouille et al. (2013) is valid.

The auto-correlation power spectrum for the galaxy survey $P_g(k, \mu)$ is

$$P_g(k, \mu) = (b_g + f \mu^2)^2 P_m(k) + \frac{1}{\bar{n}_g}, \quad (13)$$

where P_m is the matter power spectrum, and \bar{n}_g is the effective source density in the galaxy survey. The cross-correlation of the Lyman- α forest and galaxy survey $P_\times(k, \mu)$ can be written as

$$P_\times(k, \mu) = (b_F(k, \mu) + b_\eta f \mu^2) (b_g + f \mu^2) P_m(k). \quad (14)$$

Note that by crossing the two different tracers, the shot noise terms in auto-correlations have been removed. (The shot noise term in the UVB source $1/\bar{n}_j$ would be dominated by quasars since they are rare and bright. If we had used quasars as the cross-correlation tracer, then there would be a common shot noise term that depends on the overlap of the UVB quasars and the tracer quasars, described by an additional parameter; see Pontzen 2014.) For two UVB source parameters b_j and \bar{n}_j , the cross-correlation power spectrum will only be sensitive to the former. So the cross-correlation measurement could help break degeneracy between b_j and \bar{n}_j .

2.3 Fisher matrix

We derive the detection sensitivity of cross-correlation between Lyman- α and galaxy surveys to the scale-dependent UVB model under the frame of Fisher matrix formalism. Given data vector $\vec{D} = (\delta_g, \delta_F)$ and parameter vector \vec{p} , the covariance matrix is

$$\mathbf{C}(k, \mu) = \begin{pmatrix} P_g(k, \mu) & P_\times(k, \mu) \\ P_\times(k, \mu) & P_F(k, \mu) \end{pmatrix}. \quad (15)$$

The Fisher matrix for the measurement of a single mode is

$$F_{ij} = \frac{1}{2} \text{Tr} \left[\mathbf{C}^{-1} \frac{\partial \mathbf{C}}{\partial p_i} \mathbf{C}^{-1} \frac{\partial \mathbf{C}}{\partial p_j} \right]. \quad (16)$$

Summing over all available modes in the comoving survey volume V_{sur} , the Fisher matrix is

$$F_V \simeq \frac{V_{\text{sur}}}{4\pi^2} \int_{k_{\text{min}}}^{k_{\text{max}}} k^2 dk \int_{-1}^1 d\mu F(k, \mu), \quad (17)$$

where $V_{\text{sur}} = \frac{1}{3} \Omega [D_\Lambda^3(z_{\text{max}}) - D_\Lambda^3(z_{\text{min}})]$ is the comoving survey volume in the flat Universe ($\Omega_K = 0$) we assume in this work, D_Λ is the comoving angular diameter distance.

The Fisher matrix calculation is sensitive both to the small-scale and large-scale cutoffs in the k integral, since linear bias parameters are best constrained from the large number of modes at high k but the ionizing background fluctuation parameters have the largest effect at low k . We choose $k_{\text{max}} = 0.2 h \text{ Mpc}^{-1}$ as the fiducial linearity cut-off. We set a fiducial large-scale cutoff $k_{\parallel, \text{min}}$ by requiring one wavelength across the redshift shell we are using,

$$k_{\parallel, \text{min}} = \frac{2\pi}{D_\Lambda(z_{\text{max}}) - D_\Lambda(z_{\text{min}})}. \quad (18)$$

In principle, the survey also has a finite extent in the transverse direction, which could in principle lead to a survey area-dependent $k_{\perp, \text{min}}$. However, the angular size of a survey that corresponds to a ‘‘cube’’ in redshift space is $[c\Delta z/D(z)H(z)]^2 \text{ sr}$, which corresponds to 37 deg^2 for our fiducial redshift range. Since all of the planned surveys have contiguous area that is much larger than this, we have included only the radial finite size effects.

In the fiducial calculation of Fisher matrix, we have a redshift bin centered at $z = 2.4$ and spanning $2.15 < z < 2.65$, 20 logarithmically spaced k -bins from 0.01497 to $0.2 h \text{ Mpc}^{-1}$, and μ -bins with $|\mu| \geq \mu_{\text{min}} = k_{\parallel, \text{min}}/k$ for each k and $\Delta\mu = 0.1$.

The ongoing DESI 3D correlation function analysis uses a cut in real space, $r_{\text{max}} = 180 h^{-1} \text{ Mpc}$ (as was done in the eBOSS analysis; du Mas des Bourboux et al. 2020); we note that $\pi/r_{\text{max}} \approx 0.017 h \text{ Mpc}^{-1}$, which is not far from our fiducial cut. If one were to do a fit in correlation function space, it is still necessary to take into account that the continuum fitting procedure effectively high pass filters the Lyman- α forest, thereby suppressing any smooth component in the correlation function; previous analyses have taken this into account by applying this filtering to the theoretical correlation function before comparing with the data. This filtering is carried out by the D_{AB} matrix in the BOSS/eBOSS analyses (Bautista et al. 2017; de Sainte Agathe et al. 2019; du Mas des Bourboux et al. 2020). While D_{AB} describes the full filtering, we can get a simple estimate by noting that if we have a Fourier mode with some radial wave number k_{\parallel} , and project out the best-fit polynomial of order N over a skewer of length L , the variance is reduced by a factor

$$f_D = 1 - \sum_{\ell=0}^N (2\ell + 1) \left[j_\ell \left(\frac{k_{\parallel} L}{2} \right) \right]^2, \quad (19)$$

where j_ℓ represents the spherical Bessel function. (A proof of this result is provided in Appendix A.) The recent eBOSS analysis has $N = 1$ and skewers of mean length $L = 222 h^{-1} \text{ Mpc}$ (mean wavelength range $\Delta \log_{10} \lambda = 0.049$ per skewer based on the pixel counts Table 1 of du Mas des Bourboux et al. 2020), leading to $f_D = 0.8$ at $k_{\parallel} = 0.031 h \text{ Mpc}^{-1}$; $f_D = 0.1$ at $k_{\parallel} = 0.014 h \text{ Mpc}^{-1}$; and $f_D = 0.01$ at $k_{\parallel} = 0.0076 h \text{ Mpc}^{-1}$. It is evident that the filtering removes the very large low- k peak contributed from the shot noise term (top panel of Fig. 1). However a DESI×Roman analysis will presumably use a future version of

the continuum fitting and there may be some improvement in the handling of the largest-scale modes (Bautista et al. 2017). We are not certain how much improvement to expect, so in what follows we will consider forecasts where the large-scale cut is varied.

2.4 Combining surveys

In our calculation, the final Fisher matrix summing over information from cross-correlated survey strategy is built from 5 basic Fisher matrices calculated by the similar machinery described above:

- $F_{Ly\alpha \times Gal, fid}$: The information matrix from Lyman- α and galaxy survey cross-correlated area with fiducial galaxy survey strategy. In our case, fiducial and deep galaxy survey strategies differ by deep survey has longer exposure time and thus larger number of \bar{n}_g and smaller Poisson noise for power spectrum. We describe the galaxy survey strategy in detail in § 3.1.

- $F_{Ly\alpha \times Gal, deep}$: The information matrix from Lyman- α and galaxy survey cross-correlated area with deep galaxy survey strategy.

- $F_{Ly\alpha}$: The information matrix from Lyman- α forest survey only area. We implement it by setting $\bar{n}_g = 10^{-12} h^3 \text{Mpc}^{-3}$ in Eq. (13) to bury information from galaxy survey under noise such that effectively only Lyman- α forest provides information about cosmology.

- $F_{Gal, fid}$: The information matrix from galaxy survey only area with the fiducial galaxy survey strategy. We implement this by setting $P_F^{noise} = 10^{12} h^{-1} \text{Mpc}$ in Eq. 10 to cover the information from Lyman- α forest survey.

- $F_{Gal, deep}$: The information matrix from galaxy survey only area with the deep galaxy survey strategy.

The total information matrix from the combined surveys is

$$F_{tot, fid(deep)} = F_{Ly\alpha \times Gal, fid(deep)}(\Omega_{cross}) + F_{Ly\alpha}(\Omega_{Ly\alpha}) + F_{Gal, fid(deep)}(\Omega_{Gal}) + F_{prior} \quad (20)$$

where Ω_{cross} is overlapping survey area solid angle, $\Omega_{Ly\alpha}$ is the Lyman- α forest survey only area angle, and Ω_{Gal} is the galaxy survey only area angle. We include a prior information matrix F_{prior} , with choices described in Section 3.2.

3 SURVEY AND MODEL PARAMETERS

3.1 DESI and Roman

In this work, we benchmark our model by producing a realistic Lyman- α flux and galaxy cross-correlation between the Lyman- α Forest measurement of DESI and the high latitude spectroscopic survey (HLSS; Wang et al. 2022) of Roman at the overlapping redshifts $2.15 < z < 2.65$.

For Roman, we consider both a “fiducial” and “deep” [O III] emitter number density. Both of these densities are based on the Exposure Time Calculator v19 (Hirata et al. 2012). We assumed the average of the luminosity functions from grism (Colbert et al. 2013; Mehta et al. 2015) and narrow-band (Khostovan et al. 2015) surveys (model 1992 in the ETC). We used an updated throughput table based on the Phase C payload design¹ and a signal-to-noise

ratio threshold of 6. The “fiducial” number density corresponds to the reference exposure count and duration of 6×297 s; and the “deep” number density corresponds to observations twice as long (6×594 s).

For the DESI Lyman- α forest survey, we quote quasar number density in Table 2.7 of DESI Collaboration et al. (2016) for $\bar{n}_{Ly\alpha}$ in Eq. (10). We use the typical signal-to-noise ratio for DESI quasar spectra of $S/N = 2$ per re-sampled spectral pixel of width $\Delta\lambda_{obs} = 0.8 \text{ \AA}$. DESI is conducting its survey over 14,000 square degrees, split among the North and South Galactic caps; the declination range in the North Galactic Cap is $\delta > -8.2^\circ$, and that in the South Galactic Cap is $-18.4^\circ < \delta < +30^\circ$. By drawing 4×10^6 Monte Carlo samples from the sky, we find that 40,274 fall into the overlap of the reference Roman footprint and the DESI survey area, thus under the Reference survey plan they would overlap for $\Omega \approx 415.4 \text{ deg}^2$ in the sky. We show in Sec. 4 how varying survey strategy would improve the sensitivity to large-scale ionizing background parameters.

3.2 Parameter fiducial value and priors

In this work, we explore the cross-correlation strategy constraints on the 10 model parameters as collected in the upper portion of Table 1.

Here we describe physical meaning, and the choice of fiducial values and prior uncertainties (if any) at $z = 2.4$ for each parameter. Much of this builds on the choices in Pontzen (2014), but there are some updates. We use the tabulated mean UVB estimated in Haardt & Madau (2012) for fiducial values as they enter into the calculation of p_{clump} , β_r , $b_{HI, u}$.

- $\kappa_{HI} = (\beta_{clump} + \beta_{HI})\kappa_{tot} = \bar{\sigma}_{HI}n_{HI} + \bar{\kappa}_{clump}$: The physical Lyman-limit opacity, which is related to Lyman-limit photon mean free path λ_{mfp} by $\kappa_{HI} = 1/\lambda_{mfp}$. We take a fiducial value $\lambda_{mfp} = 147 \text{ Mpc}$ at $z = 2.4$ as measured by Rudie et al. (2013). There is a strong degeneracy between κ_{HI} and the ionizing source parameters (Pontzen et al. 2014), since $S(k) \propto k^{-1}$ over most of the observable range of k and the scale and amplitude are exactly degenerate for a power law. Thus the incorporation of some external information on κ_{HI} is necessary. We take the uncertainties in the measurement of opacity in Rudie et al. (2013), which breaks the uncertainty $\sigma_{\kappa_{HI}}$ into the opacity uncertainties for Lyman-limit system $\sigma_{\kappa, LLS}$ and forest opacity $\sigma_{\kappa, for}$:

$$\sigma_{\kappa_{HI}} = \sqrt{\sigma_{\kappa, LLS}^2 + \sigma_{\kappa, for}^2} \approx 0.00078 \text{ Mpc}^{-1}. \quad (21)$$

(The conversion to $h \text{ Mpc}^{-1}$ occurs inside the Fisher code.)

- $p_{clump} = \beta_{clump}/(\beta_{clump} + \beta_{HI})$: The fractional opacity contributed by clumping regions within the total opacity of intergalactic H I and clumps. To find a fiducial value of this parameter, as shown in § II.A of Pontzen (2014), at first one needs to identify the critical H I column density that distinguishes IGM and clumping regions by finding the cross point between curves of IGM H I photoionization rate and the collisional ionization rate in clumps. Thereafter, an estimation of p_{clump} is made by checking the measured fraction of IGM contributed opacity for a certain H I column density in Figure 10 of Rudie et al. (2013). The simple uniform-density 1D clump model in Pontzen (2014) gives a column density $N \approx 10/\bar{\sigma}_{HI} \approx 2.6 \times 10^{18} \text{ cm}^{-2}$. We extend the analysis to a 2D clump model (see Appendix B for details of the modeling and estimation) in order to get an estimation of uncertainty for p_{clump} . We find in the 2D model gives the column density a factor of 1/2, that is, $N \approx 1.3 \times 10^{18} \text{ cm}^{-2}$. Then the IGM should contribute

¹ Accessible at the Roman Space Telescope website: https://roman.gsfc.nasa.gov/science/RRR/Roman_effarea.20210614.xlsx

Table 2. Summary of fiducial value, priors and forecast 1σ sensitivity with the fiducial survey strategy at $z = 2.4$ and overlap area of $\Omega_{\text{cross}} = 415 \text{ deg}^2$. We show the forecast for our fiducial k -range, and for two extended k -ranges: one where k_{max} is doubled to $2 \times 0.2h \text{ Mpc}^{-1}$, and one where $k_{\parallel, \text{min}}$ is halved to $\frac{1}{2} \times 0.01497h \text{ Mpc}^{-1}$. In the last two columns, we show the improvement in constraint that could be obtained with this extension of the k -range.

Parameter	Unit	Fiducial Value	Prior 1σ	Forecast 1σ			Improvement	
				Fiducial	$k_{\text{max}} \times 2$	$k_{\parallel, \text{min}} / 2$	$k_{\text{max}} \times 2$	$k_{\parallel, \text{min}} / 2$
<i>Constrained Parameters</i>								
b_j	-	3	-	0.456	0.423	0.424	7.2%	7.0%
$1/\bar{n}_j$	$h^{-3} \text{ Mpc}^3$	1.36×10^4	-	1.665×10^4	1.437×10^4	0.895×10^4	13.4%	44.1%
$b_{\text{F}\delta}$	-	-0.1116	-	0.00099	0.00074	0.00078	25.2%	21.3%
b_η	-	-0.1594	-	0.00143	0.00098	0.00122	31.5%	14.4%
b_g	-	2.4	-	0.00592	0.00387	0.00575	34.7%	2.9%
<i>Unconstrained Parameters</i>								
p_{clump}	-	0.09	0.02	0.02	0.02	0.02		
κ_{HI}	Mpc^{-1}	0.0068	0.00078	0.00078	0.00078	0.00078		
$b_{\text{HI}, \text{u}}$	-	1.6	0.2	0.2	0.2	0.2		
β_r	-	0.3997	0.00796	0.00796	0.00796	0.00796		
b_{clump}	-	1.6	0.2	0.2	0.2	0.2		

Table 3. Summary of parameter constraints improvement in DESI+Roman going from disjoint ($\Omega_{\text{cross}} = 0$) to maximal overlap ($\Omega_{\text{cross}} = 2227 \text{ deg}^2$).

Parameter	Unit	Fiducial galaxy survey			Deep galaxy survey		
		Forecast 1σ		Improvement	Forecast 1σ		Improvement
		Disjoint	Maximal		Disjoint	Maximal	
b_j	-	0.653	0.410	37.2%	0.653	0.405	37.9%
$1/\bar{n}_j$	$h^{-3} \text{ Mpc}^{-3}$	3.814×10^4	0.888×10^4	76.7%	3.814×10^4	0.795×10^4	79.2%
$b_{\text{F}\delta}$	-	0.00151	0.00083	45.0%	0.00151	0.00079	47.7%
b_η	-	0.00230	0.00117	48.9%	0.00230	0.00112	51.1%
b_g	-	0.00594	0.00585	1.5%	0.00430	0.00423	1.6%

opacity for around 89% – 94% so we choose 0.09 as the fiducial value for p_{clump} and 0.02 as the prior uncertainty.

- $b_{\text{HI}, \text{u}}$: The bias of HI in uniform UVB limit. We follow the discussion in Pontzen (2014) for this value, while the HI number density $n_{\text{HI}} \propto \alpha(T)\rho^2$, the IGM equation-of-state $T \propto \rho^{\gamma-1}$ and recombination coefficient $\alpha(T) \propto T^{-0.7}$ (the exponent ranges from -0.74 at $T = 8 \times 10^3 \text{ K}$ to -0.66 at $T = 2 \times 10^4 \text{ K}$; Pequignot et al. 1991), this bias could be estimated by

$$b_{\text{HI}, \text{u}} = \frac{\delta n_{\text{HI}, \text{u}}}{\delta \rho} = 2 - 0.7(\gamma - 1), \quad (22)$$

where $\gamma = 1.6$ for a photo-heated IGM long after a reionization event (see McQuinn & Upton Sanderbeck 2016 for a thorough discussion), and thus giving a fiducial $b_{\text{HI}, \text{u}}$ value of 1.6. We choose the prior uncertainty for this bias as $\sigma_{b_{\text{HI}, \text{u}}} = 0.2$ (i.e., $\sigma_\gamma = 0.29$), given that He II reionization could leave a significant imprint at this redshift (Upton Sanderbeck et al. 2016; Hiss et al. 2018; Walther et al. 2019).

- β_r : The fraction of Lyman-limit photons from HI recombinations. We use Eq. 18 of Pontzen (2014) and forest temperature measurement in Becker et al. (2011) to estimate this value. The prior uncertainty is determined by $\sigma_{\beta_r} = (\partial \beta_r / \partial T) \Delta T$.

- b_{clump} : The bias of the clumps. Similar to Pontzen (2014), we assume $b_{\text{clump}} = b_{\text{HI}, \text{u}}$, $\sigma_{\text{clump}} = \sigma_{\text{HI}, \text{u}}$. The uncertainty in b_{clump} is degenerate with the uncertainty in b_j since they both enter through $b_{j, \text{eff}}$.

- b_j : The effective bias of photon source objects. This bias is an effective quantity taking emissivity contributed by multiple source

populations into account

$$b_j = \sum_{\text{source } i} \frac{j_{0, \text{source } i}}{j_0} b_{j, \text{source } i} \quad (23)$$

where $j_0 = \sum_{\text{source } i} j_{0, \text{source } i}$ is the total emissivity. The value of b_j depends on the underlying source populations. The main interest of this work is to explore the constraint on b_j by Lyman- α and galaxy cross-correlation. We follow the default value $b_j = 3.0$ in Pontzen (2014) assuming an average contribution from highly biased quasars and a range of galaxy luminosities. We leave it as a free parameter (formally, the prior $\sigma_{b_j} = \infty$).

- $1/\bar{n}_j$: The effective inverse of source number density, also shot noise contribution to power spectrum

$$\frac{1}{\bar{n}_j} = \sum_{\text{source } i} \left(\frac{j_{0, \text{source } i}}{j_0} \right)^2 \frac{1}{\bar{n}_{\text{source } i}}. \quad (24)$$

We use the inverse number density since the flux power spectrum formula is smooth even as $1/\bar{n}_j \rightarrow 0$; thus we expect the Fisher matrix approximation to be much better using $1/\bar{n}_j$ as a parameter than \bar{n}_j . Pontzen (2014) gives an approximate estimation of $2 \times 10^{-5} h^3 \text{ Mpc}^{-3} < \bar{n}_j < 10^{-4} h^3 \text{ Mpc}^{-3}$. We begin with a model with $\bar{n}_j = 5 \times 10^{-5} h^3 \text{ Mpc}^{-3}$, which translates to $1/\bar{n}_j = 2 \times 10^4 h^{-3} \text{ Mpc}^3$. However, a finite quasar lifetime would be expected to reduce the effective shot noise on large scales since over a finite light-travel time one would average over many realizations of the shot noise (Gontcho A Gontcho et al. 2014; Meiksin & McQuinn 2019). We quantify this issue in Appendix C; the factor f_{FL} by which the shot noise is sup-

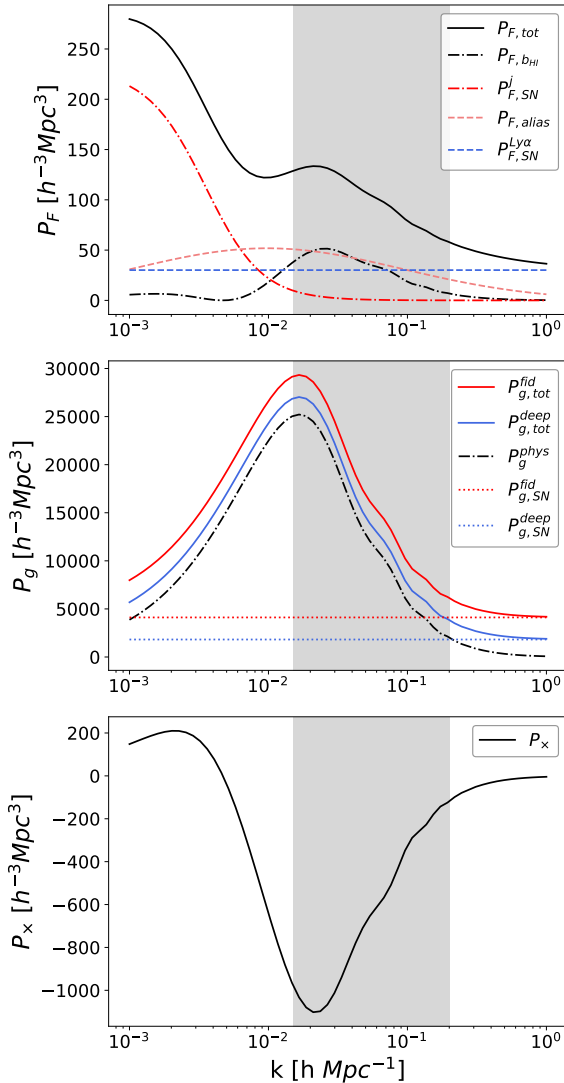


Figure 1. (Upper panel) power spectrum of Lyman- α forest flux. Black solid line is the total power spectrum; black dash dot line is the theoretical power spectrum take UVB source contribution into account; red dash dot line represents the contribution from UVB source number shot noise; the blue and coral dashed line represents the Lyman- α shot noise from detector noise and alias term respectively. (Middle panel) galaxy power spectrum with fiducial and deep survey strategy. Red solid and dotted line represents the total and shot noise power spectrum respectively for fiducial exposure time, while the blue lines corresponds to results with longer exposure time (deep survey). The black dash-dotted line is the theoretical galaxy power spectrum. (Lower panel) cross-correlated power spectrum of Lyman- α forest flux and galaxy survey. The grey blocks represents the available k range in the search of surveys.

pressed depends on the quasar lifetime t_Q , the scale k , and the angle to the line of sight μ (since with time dependent effects the light travel time to the observer is also important). At the largest scale we use ($k = 0.015 h \text{ Mpc}^{-1}$, $\mu = 1$) and a quasar lifetime of $t_Q = 100 \text{ Myr}$, the suppression factor is $f_{\text{FL}} = 0.55$. This could be smaller for even shorter quasar lifetimes, but is also larger if we consider larger k (i.e., not exactly at our minimum value). Thus we take a suppression factor corresponding to $k = 0.02 h \text{ Mpc}^{-1}$, $\mu = 1$, $t_Q = 100 \text{ Myr}$, i.e., $f_{\text{FL}} = 0.68$, or an effective

$1/\bar{n}_j = 0.68 \times 2 \times 10^4 h^{-3} \text{ Mpc}^3 = 1.36 \times 10^4 h^{-3} \text{ Mpc}^3$, as our fiducial value. We leave it as a free parameter.

- $b_{\text{F}\delta}$: The bias of Lyman- α flux to matter overdensity. The fiducial values are taken from the fiducial simulation of Arinyo-i-Prats et al. (2015). We found that the statistical errors from the DESI survey are below the current theory uncertainty of the bias parameters (Arinyo-i-Prats et al. 2015), especially if we try to marginalize over the temperature-density relation parameters, so imposing a prior does not significantly improve the constraints. Thus we took the conservative option of leaving it as a free parameter.

- b_η : The bias of Lyman- α flux to peculiar velocity gradient. Again the fiducial value is from the fiducial simulation of Arinyo-i-Prats et al. (2015) and we leave b_η as a free parameter.

- b_g : The galaxy bias. We set the fiducial value equal to 2.4 (Pontzen 2014) and regard it as a free parameter, expecting the auto-correlation in the galaxy survey to constrain it very well (at fixed cosmology).

4 RESULTS

4.1 Power Spectra

We display our results for the baseline DESI+Roman surveys for P_g , P_F , P_x in Eqs. (13–14) at $z = 2.4$, $\mu = 1/\sqrt{3}$ in Figure 1. We paint by grey shadow the available survey wavenumber region used in this work, i.e. $0.01497 \leq k \leq 0.2 h \text{ Mpc}^{-1}$. The Lyman- α flux power spectrum breaks into contribution from 3 pieces: the contribution from the first two terms of Eq. (10) corresponding to physical fluctuations in the Lyman- α transmission $P_{\text{F},\text{bHI}}$; the observational noise in the spectra $P_{\text{F}}^{\text{noise}}/\bar{n}_{\text{Ly}\alpha}$; and the aliasing term $P_{\text{F}}^{\text{LD}}/\bar{n}_{\text{Ly}\alpha}$. Note that the cross-correlation power spectrum is negative at most scales because the magnitude of flux transmission is anti-correlated with the galaxy density. However, at extremely large scales, P_x becomes positive: overdensities of matter (hence overdensities in the tracer galaxies since $b_g > 0$) have higher ionizing photon emissivity and higher ionizing background. Therefore, in ultra-large-scale overdense regions, the Lyman- α flux transmission is indeed reduced by the increased gas density, but at the same time is increased by the stronger UVB. The latter effect wins out at the largest scales where $S(k) > b_{\text{HI,u}}/b_{j,\text{eff}}$.

We display the variation of scale-dependent H I bias b_{HI} and P_F with respect to the effective source bias b_j in Figure 2. We also plot the uniform UVB scenario for comparison. At the scale of $k \approx \kappa_{\text{tot}} = 0.0100 h \text{ Mpc}^{-1}$, the flux power spectra show a sharp dip since b_{HI} crosses zero. This feature also reflects the transition of transmitted flux from matter density dominated to UVB source dominated when goes to larger scales. At the far left side of Figure 2, as $k \rightarrow 0$, the matter clustering goes away entirely, $P(k) \rightarrow 0$, and the large scale power spectrum approaches a constant given by the source shot noise term in Eq. (10) with $S(k) \rightarrow 1$.

Reflecting the Poisson fluctuation of the ionizing source number density, \bar{n}_j could impact the large scale $P_F(k)$ as well. We show the variation of P_F with respect to \bar{n}_j in Figure 3. At very large scales $k \lesssim 0.007 h \text{ Mpc}^{-1}$, the scale dependence of the \bar{n}_j is very different from the b_j effect; however this scale is outside the scale cut because of the radial width of the redshift slice. Cross-correlating the Lyman- α flux field with the galaxy field can help break this degeneracy.

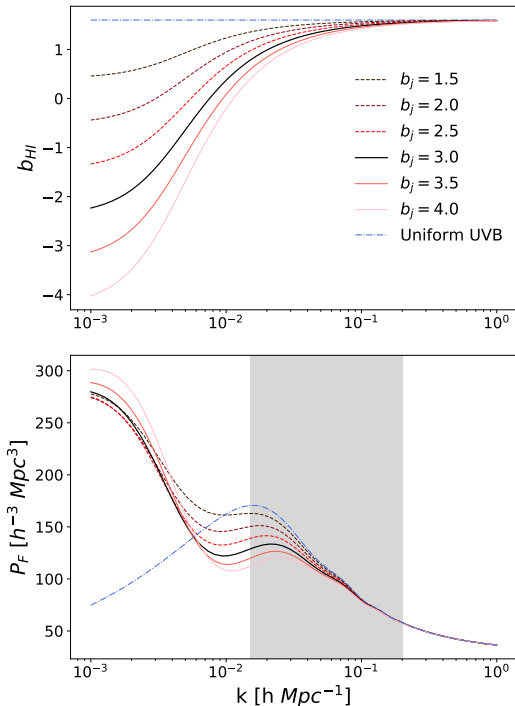


Figure 2. Variations of scale-dependent HI bias $b_{\text{HI}}(k)$ (upper panel) and Lyman- α forest flux power spectrum $P_{\text{F}}(k)$ with respect to varied effective ionizing source bias b_j at $z = 2.4$, $\mu = 1/\sqrt{3}$. The blue dash-dot line shows the spatially uniform UVB scenario for comparison. At the upper panel stronger clustering of UVB sources (larger b_j) suppresses the value of b_{HI} and shifts the zero point of it to smaller scales (larger k) because the enhancement of ionizing emissivity. At the lower panel the peak amplitude of P_{F} is suppressed and the dip is sharper also because UVB source radiation overcompensates the matter clustering.

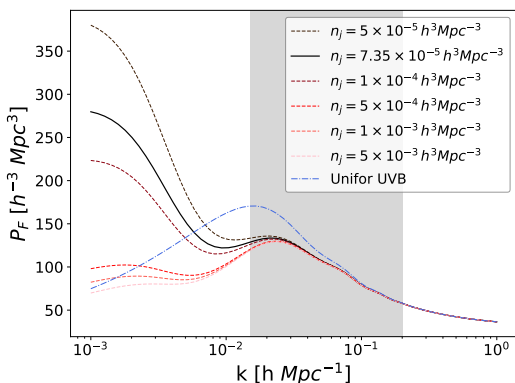


Figure 3. Variation of Lyman- α forest flux power spectrum $P_{\text{F}}(k)$ with respect to varied effective ionizing source mean number density \bar{n}_j . The shot noise of ionizing source number gives rise to the large magnitude at large scales, as also shown in upper panel of Figure. 1.

4.2 Constraints on Parameters

We list the parameter fiducial values, priors and forecasted 1σ uncertainties at $z = 2.4$, with fiducial overlapping area $\Omega_{\text{cross}} = 415 \text{ deg}^2$ in Table 2. We group the parameters by whether they are totally determined by prior knowledge. As shown in the table, the constraints on $\{p_{\text{clump}}, \kappa_{\text{HI}}, b_{\text{HI,u}}, \beta_{\text{r}}, b_{\text{clump}}\}$ are mostly determined by their priors and can be hardly improved by this observation strategy. On the other hand, the survey indeed puts constraints on the two ionizing source parameters b_j , $1/\bar{n}_j$, two Lyman- α flux bias $b_{\text{F}\delta}$, b_{η} and the galaxy bias b_{g} .

To explore possible survey strategy optimization that could be implemented by DESI or Roman, we plot the forecast error bars on the parameters with respect to overlapping survey area Ω_{cross} and the two different Roman galaxy survey exposure durations in Figure 5. For the fiducial galaxy survey scenario, we find from no overlap ($\Omega_{\text{cross}} = 0 \text{ deg}^2$) to maximum overlapping area ($\Omega_{\text{cross}} = 2227 \text{ deg}^2$) where the Roman footprint is fully contained within DESI, the detection sensitivity improvement for b_j is 37.2% from 0.653 to 0.410, for $1/\bar{n}_j$ it is 76.7% from $3.814 \times 10^4 h^{-3} \text{ Mpc}^3$ to $0.888 \times 10^4 h^{-3} \text{ Mpc}^3$. Due to the reduction of cosmic variance by cross-correlation, and the breaking of partial degeneracies² with the source shot noise $1/\bar{n}_j$, the constraints on the biasing parameters $b_{\text{F}\delta}$ and b_{η} are also mildly improved by 45.0% (0.00151 to 0.00083) and 48.9% (0.00230 to 0.00117) respectively.

The breaking of the degeneracy between b_j and $1/\bar{n}_j$ is shown in Figure 4. The ellipses show the successive decrease in the forecast 68% error ellipse as the overlap region between the two surveys is increased. The ellipse is of course a projection of a higher-dimensional ellipsoid in parameter space; as one goes beyond $\sim 1000 \text{ deg}^2$ of overlap, other directions not constrained by the cross-correlation dominate the error region in the $(b_j, 1/\bar{n}_j)$ plane, and there is only slight further improvement in the marginalized parameters. The dotted line in Fig. 4 shows the boundary of the unphysical region ($1/\bar{n}_j < 0$). In a Markov Chain Monte Carlo parameter analyses, one could add a step function prior on $1/\bar{n}_j$ to exclude the unphysical values.³ However, the use of asymmetric priors could at the same time induce biased inference for other parameters, e.g., it is more likely to have larger inferred value for b_j than smaller ones because of the orientation of the contour in Figure. 4. To avoid such issues in our forecast, we prefer to show the “full” measurement error before any such prior on $1/\bar{n}_j$ is applied.

4.3 Impact of scale cuts

We test the impact of scale cuts on our results by doubling k_{max} to $0.4 h \text{ Mpc}^{-1}$, or halving $k_{\parallel, \text{min}}$ to $k_{\parallel, \text{min}} = 0.007485 h \text{ Mpc}^{-1}$. We present the resulting changes in sensitivity in Table 2.

We find the constraining power improves when extending k_{max} . Even though the UVB parameters will be highly degenerate at the high- k regime because UVB fluctuation is a large-scale effect. The UVB parameters constraints changes a bit (7.2% for b_j and 13.4% for $1/\bar{n}_j$). This is because the number of modes increases proportional to k^3 and thus there is still non-negligible

² The correlation coefficients $\text{Corr}(b_{\text{F}\delta}, 1/\bar{n}_j)$ and $\text{Corr}(b_{\eta}, 1/\bar{n}_j)$ are +0.82 and -0.85 , respectively, for the disjoint case; for the maximal overlap case, these are reduced to +0.22 and -0.22 .

³ This could also be done in post-processing, since addition of a step function prior is equivalent to eliminating the unphysical region and normalizing the posterior probability to integrate to unity.

information contributed by higher k modes to the Fisher matrix. Other parameters get better constraints (25.2%, 31.5%, 34.7% for $b_{F\delta}$, b_η , b_g respectively) simply because they have information from smaller-scale modes.

With access to larger-scale modes while $k_{\parallel, \min}$ is reduced in our convergence test, the degeneracy of UVB parameters is broken greatly as b_j constraint improved 7.0% and $1/\bar{n}_j$ improved 44.1%. We note that for shorter quasar lifetimes, the shot noise at small k is reduced, so in that case the extension to smaller $k_{\parallel, \min}$ may lead to a smaller improvement. The improvement for $b_{F\delta}$ (21.3%), b_η (14.4%), b_g (2.9%) is not as obvious as with the information from small-scale modes.

In this paper, we show our final results in the scenario $k_{\max} = 0.2h \text{ Mpc}^{-1}$, which will be safely outside the domain of non-linear effects.

5 DISCUSSION

This work proposes to measure large-scale fluctuation of the ionizing background due to ionizing source distribution with a cross-correlation between Lyman- α forest and a galaxy survey. We make a first estimate of the cross-correlation constraints on the ionizing sources bias b_j and mean number density $1/\bar{n}_j$. We use the model in Pontzen (2014) to parameterize the ionizing source distribution in the calculation of Lyman- α flux power spectrum. The ionizing sources impact the Lyman- α flux spectrum at large scales in two ways. First, at scales larger than the mean free path of ionizing photons, the clustering of ionizing sources will compete with the clustering of matter, enhance flux transmission and suppress the power spectrum because the absolute value of H I bias is reduced. This effect is parameterized by b_j and illustrated in Figure 2. Second, the shot noise of ionizing source number density, parameterized by \bar{n}_j , will give rise to very large fluctuation and dominate the power spectrum at extreme large scale (at the far left of Figure 3). These two parameters are somewhat degenerate because they both have their main effect on large scales, although the degeneracy is not

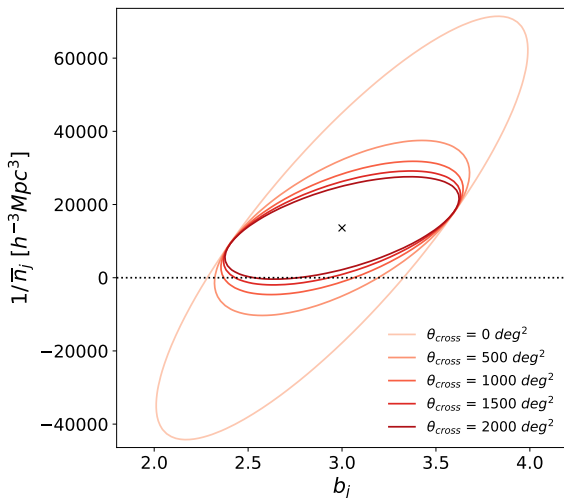


Figure 4. Projected 68% confidence ($\Delta\chi^2 = 2.3$ for 2 degrees of freedom) contours of b_j and $1/\bar{n}_j$. By increasing the overlapping area of DESI Lyman- α forest survey and Roman galaxy survey, the degeneracy between these two parameters could be reduced. The dotted line at $1/\bar{n}_j$ shows the boundary of the physical region: the portion of the model space below it is unphysical.

exact because the k -dependence of the shot noise is steeper. Cross-correlating Lyman- α flux with galaxy survey could help break this degeneracy since it could remove the shot noise term, as shown in Figure 4.

We list the forecast constraints on our model parameters by the surveys in Table 2. We find two ionizing source related parameters b_j and $1/\bar{n}_j$ could be constrained by Lyman- α forest survey. Comparing the zero overlapping and maximum overlapping area between DESI Lyman- α forest survey and Roman HLS, we find cross correlating with galaxy survey could improve the constraints, 37.2% for b_j and 76.7% for $1/\bar{n}_j$ respectively. A deeper Roman galaxy survey could also improve the constraints mildly (38% for b_j and 77 % for $1/\bar{n}_j$), although the overlap area with DESI is more important.

The model we investigate in this paper contains several simplifications, while future work could extend it to involve more complicated phenomena present in IGM. The ionizing source parameter b_j and $1/\bar{n}_j$ are both effective numbers, mixing the contributions from all source populations. In future work, assigning unique parameters to distinct source population could help identify the fraction the contribution from each of them. There are also other factors that give rise to large scale fluctuation of the IGM opacity, such as temperature fluctuation as relics of H I/He I reionization (e.g. Montero-Camacho et al. 2019) and He II reionization (McQuinn et al. 2009; Compostella et al. 2013; Greig et al. 2015). We leave the incorporation of these effects on large scale feature of IGM to future work. A full combined model of the UVB fluctuations may have to go beyond analytic approximations even at the largest scales and require a high dynamic range hydrodynamic simulation (e.g., as done in Puchwein et al. 2022 for patchy reionization) or hybrid scheme implemented on an N -body simulation (e.g., an extension of Peirani et al. 2022), which could be an exploration direction for further work. In any case, with the inclusion of these additional complications, it is likely that one would try to consider more correlations (e.g., including the Lyman- α forest, Lyman-break and IR-selected galaxies, and quasars) to see if there is a possibility of breaking the added degeneracies. The addition of other statistics such as the 3-point correlation function of the Lyman- α forest (Tie et al. 2019) might also be useful, especially in the squeezed limit where one might expect a different configuration dependence if the low- k mode is being affected by UVB fluctuations from source shot noise (the UVB is a scalar on small scales) versus a deviation correlated with the density field (whose non-linear couplings to small scales have all of the contributions in the second-order perturbation theory kernel, e.g., Fry 1984).

On the more observational/data processing side, our model contained a rather simplistic approach to the cuts at the largest scales. In agreement with the previous study by Pontzen et al. (2014), we find that the treatment of these very large scales and what modes are projected out matters. A direct comparison is difficult since Pontzen et al. (2014) worked in real space and we work in Fourier space. With κ_{HI} fixed and no marginalization over observational broadband parameters, they found $\sigma(b_j) \sim 0.12$ with Lyman- α alone (or ~ 0.15 scaled to our Δz bin), a factor of ~ 4 smaller than we find here. However, we also note that our cut is in k_{\parallel} , so the large-scale modes that we keep have large μ and thus have the largest power from density+velocity fluctuations; we have marginalized over some additional parameters; there are some subtle differences in the way the Pontzen (2014) model for intergalactic H I fluctuations was mapped onto the Lyman- α forest transmission (although both models include $b_{F\delta}$ and b_η); and the construction of the covariance matrix in the largest-scale bins

1 σ uncertainties of parameters

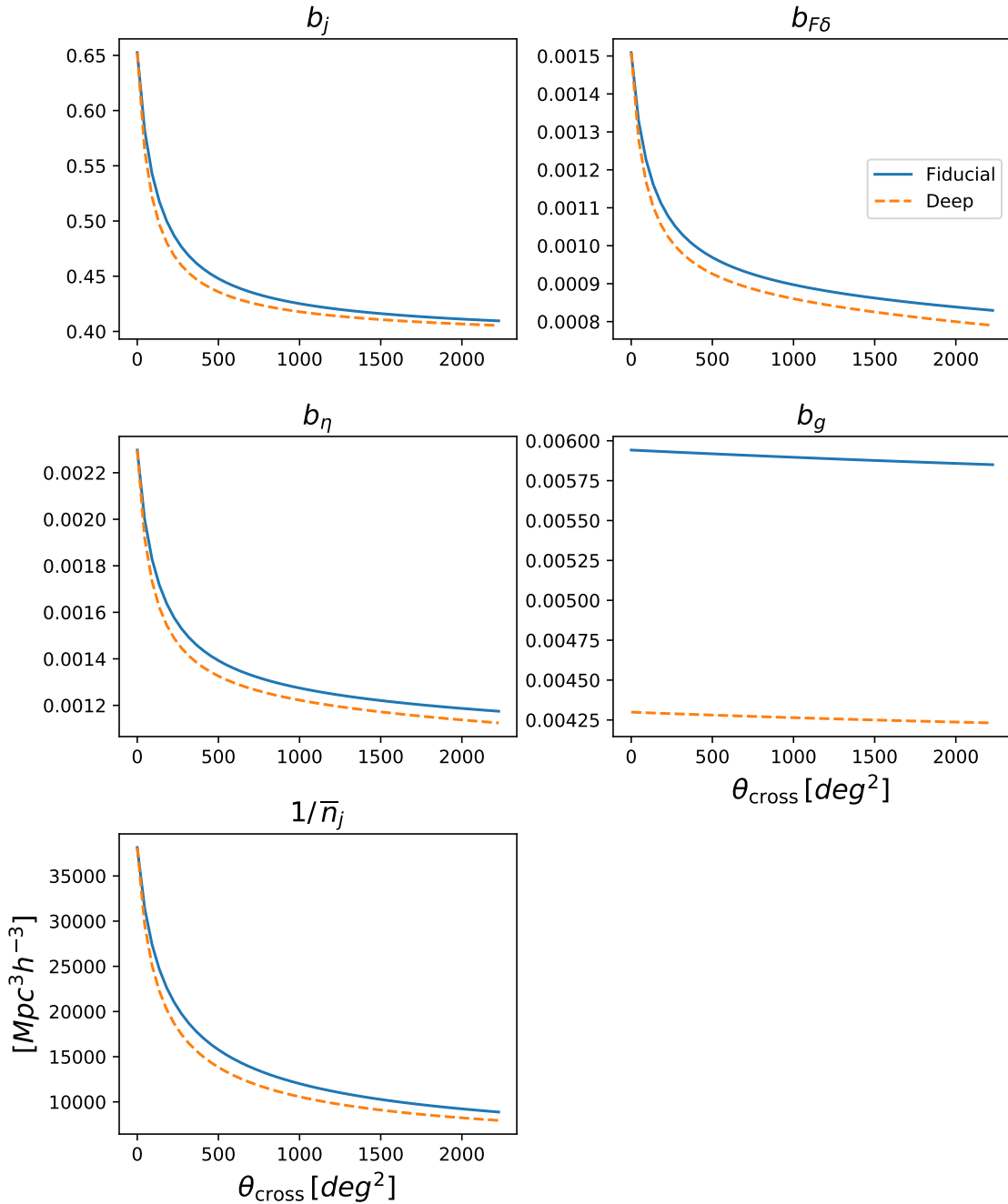


Figure 5. The 1σ parameter uncertainties as a function of θ_{cross} , the overlap area of the DESI Lyman- α forest survey and Roman galaxy survey.

is based on different assumptions. Future work should take into account the precise way in which the Lyman- α data are processed in order to predict which modes at the very largest scales are actually recovered. Our finding that these cuts matter further motivates work to model the quasar continuum and other large-scale observational systematics to maximize sensitivity to UVB physics.

For the future, other galaxy redshift surveys have been proposed that could explore this redshift range, such as the MaunaKea Spectroscopic Explorer (The MSE Science Team et al. 2019) and

MegaMapper (Schlegel et al. 2019). The basic approach of cross-correlating the Lyman- α forest with galaxy samples would be applicable to these surveys as well, although the model would have to be expanded to take into account the unique features of the other target classes selected by the Lyman break. For example, on the very large scales of interest here, where $2\pi/k_{\parallel} \sim 400h^{-1}$ Mpc is of order the separation of Lyman- α and Lyman- β , the shape and central rest frame wavelength of the Lyman break depends on the IGM density. Therefore one would have to include in the model

a line-of-sight biasing term corresponding to how the change in transmission maps onto the color cuts used. We do not anticipate any fundamental difficulties in adding this to the model, but it is beyond the scope of this work.

Our results motivate survey strategies more dedicated to probe the UVB fluctuations. We emphasize that the improvement shown in our table is just from choosing the footprint of the two surveys, neither of which has the UVB as its primary science case. There are of course practical limitations: DESI is based in the Northern Hemisphere, and especially at the bluer wavelengths used for the Lyman- α forest there is a loss of throughput as one points closer to the horizon. Roman is space-based, but the Reference Survey design (Wang et al. 2022) was driven by the need to overlap with Southern Hemisphere telescopes such as the Vera Rubin Observatory⁴, and the sky brightness (dominated by zodiacal light) increases as one moves closer to the Ecliptic (Leinert et al. 1998). The survey choices may evolve in the future as the actual survey plan for Roman is defined, and as follow-on programs are considered for DESI. The large-scale ultraviolet background fluctuations are one example illustrating how the combined footprints of surveys should be considered in assessing the overall science reach.

ACKNOWLEDGEMENTS

We thank Naim Göksel Karaçaylı, Andrei Cuceu, Paulo Montero-Camacho, and Paul Martini for useful discussion and comments in the preparation of this draft. We thank the anonymous referee for comments that improved the paper, especially regarding the finite source lifetime effects. During the preparation of this work, the authors were supported by NASA award 15-WFIRST15-0008, Simons Foundation award 60052667, and the David & Lucile Packard Foundation.

DATA AVAILABILITY

The data underlying this article will be shared on reasonable request to the corresponding author.

REFERENCES

- Abramowitz M., Stegun I. A., 1972, Handbook of Mathematical Functions
 Arinyo-i-Prats A., Miralda-Escudé J., Viel M., Cen R., 2015, *J. Cosmology Astropart. Phys.*, 2015, 017
 Bajtlik S., Duncan R. C., Ostriker J. P., 1988, *ApJ*, 327, 570
 Bautista J. E., et al., 2017, *A&A*, 603, A12
 Becker G. D., Bolton J. S., 2013, *MNRAS*, 436, 1023
 Becker G. D., Bolton J. S., Haehnelt M. G., Sargent W. L. W., 2011, *MNRAS*, 410, 1096
 Blas D., Lesgourgues J., Tram T., 2011, *J. Cosmology Astropart. Phys.*, 2011, 034
 Bolton J. S., Haehnelt M. G., 2007, *MNRAS*, 382, 325
 Bolton J. S., Haehnelt M. G., Viel M., Springel V., 2005, in Williams P., Shu C.-G., Menard B., eds, IAU Colloq. 199: Probing Galaxies through Quasar Absorption Lines. pp 219–224 (arXiv:astro-ph/0504437), doi:10.1017/S1743921305002620
 Calverley A. P., Becker G. D., Haehnelt M. G., Bolton J. S., 2011, *MNRAS*, 412, 2543
 Carswell R. F., Webb J. K., Baldwin J. A., Atwood B., 1987, *ApJ*, 319, 709
 Chen H., Gnedin N. Y., 2021, *Astrophys. J.*, 911, 60
 Colbert J. W., et al., 2013, *ApJ*, 779, 34
 Compostella M., Cantalupo S., Porciani C., 2013, *MNRAS*, 435, 3169
 Cowie L. L., Barger A. J., Trouille L., 2009, *ApJ*, 692, 1476
 Croft R. A. C., Weinberg D. H., Pettini M., Hernquist L., Katz N., 1999, *ApJ*, 520, 1
 D’Aloisio A., McQuinn M., Davies F. B., Furlanetto S. R., 2018, *MNRAS*, 473, 560
 DESI Collaboration et al., 2016, arXiv e-prints, p. arXiv:1611.00036
 Dall’Aglia A., Gnedin N. Y., 2010, *ApJ*, 722, 699
 Dall’Aglia A., Wisotzki L., Worseck G., 2008, *A&A*, 491, 465
 Dawson K. S., et al., 2013, *AJ*, 145, 10
 Faucher-Giguère C.-A., Lidz A., Hernquist L., Zaldarriaga M., 2008, *ApJ*, 688, 85
 Fry J. N., 1984, *ApJ*, 279, 499
 Gallego S. G., et al., 2021, *MNRAS*, 504, 16
 Gontcho A Gontcho S., Miralda-Escudé J., Busca N. G., 2014, *MNRAS*, 442, 187
 Greig B., Bolton J. S., Wyithe J. S. B., 2015, *MNRAS*, 447, 2503
 Haardt F., Madau P., 2012, *ApJ*, 746, 125
 Hirata C. M., Gehrels N., Kneib J.-P., Kruk J., Rhodes J., Wang Y., Zoubian J., 2012, arXiv e-prints, p. arXiv:1204.5151
 Hiss H., Walther M., Hennawi J. F., Oñorbe J., O’Meara J. M., Rorai A., Lukić Z., 2018, *ApJ*, 865, 42
 Hui L., Gnedin N. Y., 1997, *MNRAS*, 292, 27
 Kaiser N., 1987, *MNRAS*, 227, 1
 Karaçaylı N. G., Font-Ribera A., Padmanabhan N., 2020, *MNRAS*, 497, 4742
 Keating L. C., Puchwein E., Haehnelt M. G., 2018, *MNRAS*, 477, 5501
 Khaire V., et al., 2019, *MNRAS*, 486, 769
 Khostovan A. A., Sobral D., Mobasher B., Best P. N., Smail I., Stott J. P., Hemmati S., Nayyeri H., 2015, *MNRAS*, 452, 3948
 Leinert C., et al., 1998, *A&AS*, 127, 1
 McDonald P., Seljak U., 2009, *J. Cosmology Astropart. Phys.*, 2009, 007
 McDonald P., Seljak U., Cen R., Bode P., Ostriker J. P., 2005, *MNRAS*, 360, 1471
 McQuinn M., 2016, *ARA&A*, 54, 313
 McQuinn M., Upton Sanderbeck P. R., 2016, *MNRAS*, 456, 47
 McQuinn M., White M., 2011, *MNRAS*, 415, 2257
 McQuinn M., Lidz A., Zaldarriaga M., Hernquist L., Hopkins P. F., Dutta S., Faucher-Giguère C.-A., 2009, *ApJ*, 694, 842
 McQuinn M., Hernquist L., Lidz A., Zaldarriaga M., 2011, *MNRAS*, 415, 977
 Mehta V., et al., 2015, *ApJ*, 811, 141
 Meiksin A., 2005, *MNRAS*, 356, 596
 Meiksin A., McQuinn M., 2019, *MNRAS*, 482, 4777
 Meiksin A., Suarez T., 2022, *MNRAS*, 516, 572
 Mesinger A., Furlanetto S., 2009, *MNRAS*, 400, 1461
 Montero-Camacho P., Hirata C. M., Martini P., Honscheid K., 2019, *MNRAS*, 487, 1047
 Oxholm T. M., Switzer E. R., 2021, *Phys. Rev. D*, 104, 083501
 Palanque-Delabrouille N., et al., 2013, *A&A*, 559, A85
 Peirani S., et al., 2022, *MNRAS*, 514, 3222
 Pequignot D., Petitjean P., Boisson C., 1991, *A&A*, 251, 680
 Planck Collaboration et al., 2016, *A&A*, 594, A13
 Pontzen A., 2014, *Phys. Rev. D*, 89, 083010
 Pontzen A., Bird S., Peiris H., Verde L., 2014, *ApJ*, 792, L34
 Puchwein E., Haardt F., Haehnelt M. G., Madau P., 2019, *MNRAS*, 485, 47
 Puchwein E., et al., 2022, arXiv e-prints, p. arXiv:2207.13098
 Robertson B. E., 2022, *ARA&A*, 60, 121
 Romano M., Grazian A., Giallongo E., Cristiani S., Fontanot F., Boutsia K., Fiore F., Menci N., 2019, *A&A*, 632, A45
 Rudie G. C., Steidel C. C., Shapley A. E., Pettini M., 2013, *ApJ*, 769, 146
 Schlegel D., Kollmeier J. A., Ferraro S., 2019, in Bulletin of the American Astronomical Society. p. 229 (arXiv:1907.11171)
 Seljak U., 2009, *Phys. Rev. Lett.*, 102, 021302
 Spergel D., et al., 2015, arXiv e-prints, p. arXiv:1503.03757
 Steidel C. C., Bogosavljević M., Shapley A. E., Reddy N. A., Rudie G. C., Pettini M., Trainor R. F., Strom A. L., 2018, *ApJ*, 869, 123

⁴ URL: <https://www.lsst.org>

- Suarez T., Pontzen A., 2017, *MNRAS*, **472**, 2643
 The MSE Science Team et al., 2019, arXiv e-prints, p. arXiv:1904.04907
 Tie S. S., Weinberg D. H., Martini P., Zhu W., Peirani S., Suarez T., Colombi S., 2019, *MNRAS*, **487**, 5346
 Upton Sanderbeck P. R., D'Aloisio A., McQuinn M. J., 2016, *MNRAS*, **460**, 1885
 Upton Sanderbeck P., Iršič V., McQuinn M., Meiksin A., 2019, *MNRAS*, **485**, 5059
 Vanzella E., et al., 2012, *ApJ*, **751**, 70
 Walther M., Oñorbe J., Hennawi J. F., Lukić Z., 2019, *ApJ*, **872**, 13
 Wang Y., et al., 2022, *ApJ*, **928**, 1
 White M., Pope A., Carlson J., Heitmann K., Habib S., Fasel P., Daniel D., Lukic Z., 2010, *ApJ*, **713**, 383
 Wise J. H., 2019, arXiv e-prints, p. arXiv:1907.06653
 de Sainte Agathe V., et al., 2019, *A&A*, **629**, A85
 du Mas des Bourboux H., et al., 2020, *ApJ*, **901**, 153

APPENDIX A: PROJECTING A POLYNOMIAL FIT FROM A RANDOM FIELD

In this appendix, we present a proof of Eq. (19), the reduction factor f_D in variance of a 1-dimensional random field when the least squares fit polynomial is projected out.

First, let us consider a real random field $\psi(x)$ (not necessarily Gaussian), where x is a position. In our application, ψ is the transmitted flux perturbation δ_F , but the result is more general. The field has a 1D power spectrum $P_\psi(k)$, defined in the usual way by

$$\langle \tilde{\psi}^*(k)\tilde{\psi}(k') \rangle = 2\pi\delta(k-k')P_\psi(k), \quad (\text{A1})$$

and a variance

$$\text{Var}[\psi(x)] = \frac{1}{\pi} \int_0^\infty P_\psi(k) dk \quad (\text{A2})$$

that does not depend on position x .

Now we take a skewer of length L , which without loss of generality can be taken to extend over $-\frac{1}{2}L < x < \frac{1}{2}L$. We will find it convenient to expand ψ in the basis of Legendre polynomials⁵ $\mathbb{P}_\ell(2x/L)$ since they are orthogonal over the skewer:

$$\int_{-L/2}^{L/2} \mathbb{P}_\ell\left(\frac{2x}{L}\right) \mathbb{P}_{\ell'}\left(\frac{2x}{L}\right) dx = \frac{L}{2\ell+1} \delta_{\ell\ell'}. \quad (\text{A3})$$

Within the skewer, the function ψ can be expressed as

$$\psi(x) = \sum_{\ell=0}^{\infty} a_\ell \mathbb{P}_\ell\left(\frac{2x}{L}\right), \quad -\frac{1}{2}L < x < \frac{1}{2}L, \quad (\text{A4})$$

with

$$a_\ell = \frac{2\ell+1}{L} \int_{-L/2}^{L/2} \psi(x) \mathbb{P}_\ell\left(\frac{2x}{L}\right) dx. \quad (\text{A5})$$

We now want to find the polynomial ψ_{fit} of order N that fits ψ with the smallest mean square residual. We write the polynomial as $\psi_{\text{fit}}(x) = \sum_{\ell=0}^N b_\ell \mathbb{P}_\ell(2x/L)$, where the $N+1$ coefficients $b_0 \dots b_N$

⁵ Since P and L have other uses in this paper, we use \mathbb{P} to denote the Legendre polynomials.

float. The mean square residual is

$$\begin{aligned} \text{MSR} &= \frac{1}{L} \int_{-L/2}^{L/2} [\psi(x) - \psi_{\text{fit}}(x)]^2 dx \\ &= \frac{1}{L} \int_{-L/2}^{L/2} \left[\sum_{\ell=0}^{\infty} a_\ell \mathbb{P}_\ell\left(\frac{2x}{L}\right) - \sum_{\ell=0}^N b_\ell \mathbb{P}_\ell\left(\frac{2x}{L}\right) \right]^2 dx \\ &= \sum_{\ell=0}^N \frac{(a_\ell - b_\ell)^2}{2\ell+1} + \sum_{\ell=N+1}^{\infty} \frac{a_\ell^2}{2\ell+1}, \end{aligned} \quad (\text{A6})$$

where we used the orthogonality relation (Eq. A3) in the last step. The minimum is achieved when $b_\ell = a_\ell$ for $\ell = 0, 1, \dots, N$, since this sets the first term to its minimum possible value of zero. Then the mean square residual is simply the second term. Its expectation value is

$$\begin{aligned} \langle \text{MSR} \rangle &= \sum_{\ell=N+1}^{\infty} \frac{\langle a_\ell^2 \rangle}{2\ell+1} \\ &= \sum_{\ell=N+1}^{\infty} \frac{2\ell+1}{L^2} \left\langle \left| \int_{-L/2}^{L/2} \psi(x) \mathbb{P}_\ell\left(\frac{2x}{L}\right) dx \right|^2 \right\rangle \\ &= \sum_{\ell=N+1}^{\infty} \frac{2\ell+1}{L^2} \left\langle \left| \int_{-\infty}^{\infty} \frac{dk}{2\pi} \tilde{\psi}(k) \right. \right. \\ &\quad \left. \left. \times \int_{-L/2}^{L/2} dx e^{ikx} \mathbb{P}_\ell\left(\frac{2x}{L}\right) \right|^2 \right\rangle \\ &= \sum_{\ell=N+1}^{\infty} \frac{2\ell+1}{L^2} \left\langle \left| \int_{-\infty}^{\infty} \frac{dk}{2\pi} \tilde{\psi}(k) i^\ell L j_\ell\left(\frac{kL}{2}\right) \right|^2 \right\rangle \\ &= \sum_{\ell=N+1}^{\infty} (2\ell+1) \int_0^\infty \frac{dk}{\pi} P_\psi(k) \left[j_\ell\left(\frac{kL}{2}\right) \right]^2, \end{aligned} \quad (\text{A7})$$

where in the second equality we used the fact that a_ℓ is real; in the fourth equality we used the integral relating the Legendre polynomials to the spherical Bessel functions, Eq. (10.1.14) of Abramowitz & Stegun (1972); and in the final equality we used the expectation value (Eq. A1), used the δ -function to collapse one of the two copies of the k -integral, and used the even nature of the integrand to write the integral over only positive k . We may then write the ratio of the expected mean square residual to the variance of the original field:

$$\frac{\langle \text{MSR} \rangle}{\text{Var}[\psi(x)]} = \frac{\int_0^\infty P_\psi(k) f_D(k) dk / \pi}{\int_0^\infty P_\psi(k) dk / \pi}, \quad (\text{A8})$$

where the k -dependent reduction factor $f_D(k)$ is

$$f_D(k) = \sum_{\ell=N+1}^{\infty} (2\ell+1) \left[j_\ell\left(\frac{kL}{2}\right) \right]^2. \quad (\text{A9})$$

The sum rule, Eq. (10.1.50) of Abramowitz & Stegun (1972), allows us to write this instead as

$$f_D(k) = 1 - \sum_{\ell=0}^N (2\ell+1) \left[j_\ell\left(\frac{kL}{2}\right) \right]^2, \quad (\text{A10})$$

which completes the proof of Eq. (19). Note that from Eq. (A9), $f_D(k) \rightarrow 0$ as $N \rightarrow \infty$.

Another useful limiting form is that for small kL , the Taylor series for j_ℓ (Eq. 10.1.2 of Abramowitz & Stegun 1972) gives $f_D \propto (kL)^{2(N+1)}$. In particular, for $N = 1$ (linear fit) we have $f_D(k) \rightarrow \frac{1}{720} (kL)^4$.

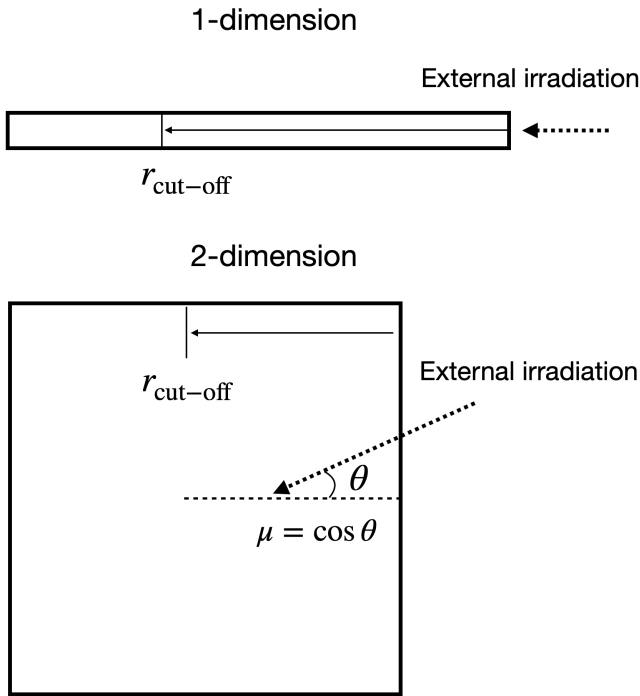


Figure B1. Illustrations for the 1D and 2D clump models we use to estimate the fraction of opacity by clumping regions and IGM H I .

APPENDIX B: 2-DIMENSIONAL CLUMP ESTIMATION OF FRACTIONAL OPACITY

We illustrate our 1-dimensional and 2-dimensional clump models (used in the estimation of p_{clump} in the main text) in Figure B1. The photoionization rate Γ_{pi} decays exponentially with the total hydrogen column density N . When irradiated by an external flux, the mean Γ_{pi} can be approximately written as

$$\Gamma_{pi} \propto \Gamma_0 \left\langle e^{-\bar{\sigma}_{\text{HI}} N(r)} \right\rangle, \quad (\text{B1})$$

where Γ_0 is the photoionization rate in the exterior.

The 1-dimensional model, most similar to the method of Pontzen et al. (2014), considers radiation only propagating along a single axis, which is also used to measure the column density. Converting the depth r inside of the clump to the fraction of cut-off column density $N_{\text{cut-off}}$, we get an estimation for the 1-dimensional clump model as follows

$$\begin{aligned} \left\langle e^{-\sigma_{\text{HI}} N(r)} \right\rangle &= \int_0^1 dx e^{-\sigma_{\text{HI}} N_{\text{cut-off}} x(r)} \\ &= \frac{1 - e^{-\bar{\sigma}_{\text{HI}} N_{\text{cut-off}}}}{\bar{\sigma}_{\text{HI}} N_{\text{cut-off}}} \\ &\approx \frac{1}{\bar{\sigma}_{\text{HI}} N_{\text{cut-off}}}, \end{aligned} \quad (\text{B2})$$

where the coordinate x ($0 < x < 1$) is the fraction of the path through the cloud ($x = 0$ at the exposed surface).

For the 2-dimensional model, there is an additional dependence on the external irradiation angle θ , which is taken to be

isotropic (uniformly distributed in $\mu = \cos \theta$):

$$\begin{aligned} \left\langle e^{-\bar{\sigma}_{\text{HI}} N(r, \mu)} \right\rangle &= \int_0^1 dx \int_0^1 d\mu e^{-\sigma_{\text{HI}} N_{\text{cut-off}} x(r)/\mu} \\ &= \int_0^1 d\mu \frac{1 - e^{-\bar{\sigma}_{\text{HI}} N_{\text{cut-off}}/\mu}}{\bar{\sigma}_{\text{HI}} N_{\text{cut-off}}/\mu} \\ &\approx \frac{1}{2\bar{\sigma}_{\text{HI}} N_{\text{cut-off}}}. \end{aligned} \quad (\text{B3})$$

This is different by a factor of 2.

We emphasize that both of these models refer to highly oversimplified geometries; their main purpose is to show how much variation in the relation between Γ_{pi} and $N_{\text{cut-off}}$ can be obtained by order-unity factors in the geometry of the cloud, and hence what is a reasonable prior uncertainty in p_{clump} .

APPENDIX C: SOURCE LIFETIMES AND THE SHOT NOISE TERM

Finite source lifetimes can reduce the quasar shot noise term in ionizing background models: if the scale of the perturbation $1/k$ is large compared to the distance a photon can travel during the quasar lifetime ct_Q/a (where t_Q is the quasar lifetime), then there is an effective increase in the number of individual sources that contribute to the ionizing background. Gontcho A Gontcho et al. (2014) modeled this in correlation function space by multiplying the shot noise term by a scale dependent factor. Meiksin & McQuinn (2019) performed a sophisticated Fourier-space calculation of the time-dependent effects. The purpose of this appendix is to provide a simple analytic estimate of the finite lifetime effects that is usable in the range of scales most of interest here ($k \sim \text{few} \times 10^{-2} h \text{ Mpc}^{-1}$). We would like to include the proper geometric factors that were alluded to in Gontcho A Gontcho et al. (2014), while having an expression that is simple to understand.

The basic question we seek to answer here is the following: suppose there is a set of sources with some mean number density $1/\bar{n}$ at any given time. These sources emit radiation into the IGM that is absorbed (or redshifted) with some mean free path κ_{tot}^{-1} . Suppose that there is a probability $p(\Delta t)$ that a source that is ‘‘on’’ at some time t is still on at time $t + \Delta t$. By what factor $f_{\text{FL}}(k, \mu)$ is the power spectrum of radiation intensity fluctuations relative to a steady-state distribution of sources? We address this question at scales small compared to the Hubble scale, $k \gg aH$, so that we can have time-dependent perturbations in the radiation intensity on a time-independent background (in the sense described in Meiksin & McQuinn 2019). We allow for a μ -dependence here because we compute the power spectrum on the light cone, i.e., allowing for the variation in look-back time as seen by the observer.

Let us suppose that the observer is looking along the z -axis (in direction \hat{e}_3). Suppose we consider a box of volume V , considering N sources of luminosity L , where source q are each on for some interval of time \mathcal{B}_q (where $q = 1 \dots N$). Then the intensity of radiation at point \mathbf{r} is

$$J(\mathbf{r}, t_0) = \sum_q \frac{L e^{-\kappa_{\text{tot}} a |\mathbf{r} - \mathbf{r}_q|}}{4\pi a^2 |\mathbf{r} - \mathbf{r}_q|^2} \chi_{\mathcal{B}_q} \left(t_0 - a \frac{r_3 + |\mathbf{r} - \mathbf{r}_q|}{c} \right), \quad (\text{C1})$$

where t_0 is the time at which light must leave the origin to reach the observer; the sum is over sources; $a|\mathbf{r} - \mathbf{r}_q|$ is the physical distance from the point of interest to the source; the inverse square law and exponential attenuation have been considered; $\chi_{\mathcal{B}_q}$ is the characteristic function that is 1 if the argument is in the interval \mathcal{B}_q

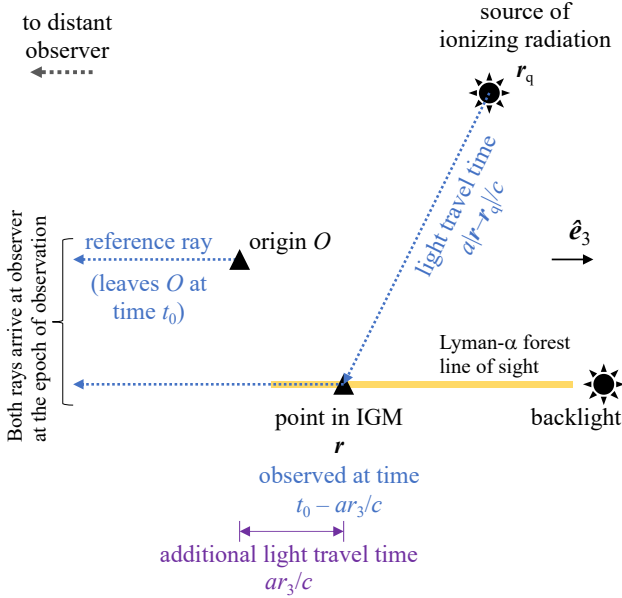


Figure C1. The geometry for the time-dependent shot noise calculation in Appendix C, showing the symbols in Eq. (C1). We work in the distant-observer approximation, with the observer looking to the right (\hat{e}_3 direction). We define an arbitrary location O to be the origin; the observer sees O as it was at some time t_0 . A given point \mathbf{r} in the Lyman- α forest is seen as it was at time $t_0 - ar_3/c$ due to the additional light travel time noted along the bottom path (note the factor of a since we work in comoving position but physical time; and that r_3 is the component of \mathbf{r} in the line of sight direction). This point \mathbf{r} is illuminated by a source at position \mathbf{r}_q , separated by a light-travel time $a|\mathbf{r} - \mathbf{r}_q|/c$. Overall, the time radiation must have left the source \mathbf{r}_q to contribute to the radiation intensity at \mathbf{r} at the relevant epoch for the distant observer is $t_0 - ar_3/c - a|\mathbf{r} - \mathbf{r}_q|/c$; therefore it is this time that appears in Eq. (C1).

and 0 otherwise; and the argument includes the point-to-observer delay and the source-to-point delay (see Fig. C1).

Equation (C1) can be simplified by using the Fourier transform of the characteristic function:

$$\chi_{\mathcal{B}_q}(t) = \int_{-\infty}^{\infty} \tilde{\chi}_{\mathcal{B}_q}(\omega) e^{-i\omega t} \frac{d\omega}{2\pi}. \quad (\text{C2})$$

The characteristic function has the correlation function

$$\langle \chi_{\mathcal{B}_q}(t) \chi_{\mathcal{B}_q}(t + \Delta t) \rangle = \frac{\bar{n}V}{N} p(\Delta t), \quad (\text{C3})$$

and so its frequency-space power spectrum is

$$\langle \tilde{\chi}_{\mathcal{B}_q}^*(\omega) \tilde{\chi}_{\mathcal{B}_q}(\omega') \rangle = 2\pi \frac{\bar{n}V}{N} \tilde{p}(\omega) \delta(\omega - \omega'), \quad (\text{C4})$$

where \tilde{p} denotes the Fourier transform of p . The steady source case would have $p(\Delta t) = 1$ and $\tilde{p}(\omega) = 2\pi\delta(\omega)$.

We also take the 3-dimensional Fourier transform of J at fixed

t_0 :

$$\begin{aligned} \tilde{J}(\mathbf{k}, t_0) &= \int_V J(\mathbf{r}, t_0) e^{-i\mathbf{k}\cdot\mathbf{r}} d^3\mathbf{r} \\ &= \int_{-\infty}^{\infty} \sum_q \int_V \frac{L e^{-\kappa_{\text{tot}} a s_q}}{4\pi a^2 s_q^2} e^{-i\omega[t_0 - a(r_3 + s_q)/c]} \tilde{\chi}_{\mathcal{B}_q}(\omega) \\ &\quad \times e^{-i\mathbf{k}\cdot\mathbf{r}} d^3\mathbf{r} \frac{d\omega}{2\pi} \\ &= L \int_{-\infty}^{\infty} \frac{d\omega}{2\pi} \sum_q e^{-i\mathbf{k}\cdot\mathbf{r}_q} e^{-i\omega(t_0 - ar_3/c)} \tilde{\chi}_{\mathcal{B}_q}(\omega) \\ &\quad \times \int_V d^3\mathbf{s}_q \frac{e^{-(\kappa_{\text{tot}} - i\omega/c) a s_q}}{4\pi a^2 s_q^2} e^{-i(\mathbf{k} - a\omega\hat{e}_3/c)\cdot\mathbf{s}_q}, \quad (\text{C5}) \end{aligned}$$

where we define $\mathbf{s}_q \equiv \mathbf{r} - \mathbf{r}_q$, and in the last line changed the integration variable to \mathbf{s}_q and split apart the terms in the exponential.

The power spectrum of J is then obtained by the usual procedure of taking the square norm of Eq. (C5), averaging, and dividing by V . Since we are considering the case of shot noise, we consider only the contributions to the square of Eq. (C5) arising from the same source. This means we can take a single source q at a random position and multiply by N . The expectation values involving $\tilde{\chi}_{\mathcal{B}_q}(\omega)$ are simplified using Eq. (C4) – this cancels the arbitrary factors of N and V , and the δ -function collapses one of the frequency integrals. The result is:

$$\begin{aligned} P_{\tilde{J}}(\mathbf{k}) &= \bar{n}L^2 \int_{-\infty}^{\infty} \frac{d\omega}{2\pi} \tilde{p}(\omega) \\ &\quad \times \left| \int_V d^3\mathbf{s}_q \frac{e^{-(\kappa_{\text{tot}} - i\omega/c) a s_q}}{4\pi a^2 s_q^2} e^{-i(\mathbf{k} - a\omega\hat{e}_3/c)\cdot\mathbf{s}_q} \right|^2. \quad (\text{C6}) \end{aligned}$$

The integral in the absolute value (which we will call \mathcal{I}) can be simplified by the usual procedure of writing it in polar coordinates. Let us define the vector

$$\mathbf{K} \equiv \mathbf{k} - \frac{a\omega}{c} \hat{e}_3. \quad (\text{C7})$$

The magnitude is

$$K = \sqrt{k^2 + \frac{a^2\omega^2}{c^2} - 2\frac{a\omega}{c} k\mu}. \quad (\text{C8})$$

Then the volume integral in Eq. (C6) can be written in polar coordinates with the ‘‘North Pole’’ pointed toward \mathbf{K} . There is an angle from the North Pole, θ (with $\bar{\mu} = \cos\theta$; we will use a bar to distinguish this from line-of-sight angle of \mathbf{k}) and a longitude $\bar{\phi}$ with trivial dependence that brings out a factor of 2π . There is also a radial integral over s_q . Then the integral is:

$$\begin{aligned} \mathcal{I} &= \frac{1}{2} \int_{-1}^1 d\bar{\mu} \int_0^{\infty} ds_q \frac{e^{-(\kappa_{\text{tot}} - i\omega/c - iK\bar{\mu}/a) a s_q}}{a^2} \\ &= \frac{1}{2a^3} \int_{-1}^1 \frac{d\bar{\mu}}{\kappa_{\text{tot}} - i\omega/c - iK\bar{\mu}/a} \\ &= \frac{i}{2a^2 K} \ln \frac{\kappa_{\text{tot}} - i\omega/c - iK/a}{\kappa_{\text{tot}} - i\omega/c + iK/a} \\ &= \frac{1}{2a^2 K} \left[\tan^{-1} \frac{K/a + \omega/c}{\kappa_{\text{tot}}} + \tan^{-1} \frac{K/a - \omega/c}{\kappa_{\text{tot}}} \right. \\ &\quad \left. + \frac{i}{2} \ln \frac{\kappa_{\text{tot}}^2 + (K/a + \omega/c)^2}{\kappa_{\text{tot}}^2 + (K/a - \omega/c)^2} \right]. \quad (\text{C9}) \end{aligned}$$

In the last line, we have used the usual rule for the logarithm of a

complex number in terms of its polar coordinates. We then arrive at a final expression for the power spectrum:

$$P_j(k, \mu) = \frac{\bar{n}L^2}{\kappa_{\text{tot}}^2 a^6} \int_{-\infty}^{\infty} \frac{d\omega}{2\pi} \tilde{p}(\omega) \mathcal{H}\left(\frac{K}{a\kappa_{\text{tot}}}, \frac{\omega}{\kappa_{\text{tot}}c}\right), \quad (\text{C10})$$

where we have defined the \mathcal{H} -function

$$\mathcal{H}(x, y) \equiv \left[\frac{\tan^{-1}(x+y) + \tan^{-1}(x-y)}{2x} \right]^2 + \frac{1}{16x^2} \left[\ln \frac{1+(x+y)^2}{1+(x-y)^2} \right]^2. \quad (\text{C11})$$

We note the limiting case

$$\mathcal{H}(x, 0) = \left(\frac{\tan^{-1}x}{x} \right)^2 = [S(a\kappa_{\text{tot}}x)]^2, \quad (\text{C12})$$

so in the time-independent case ($\omega = 0$) we recover the usual result.

Now in the time-independent case, $\tilde{p}(\omega) = 2\pi\delta(\omega)$, the power spectrum then collapses to $\bar{n}L^2[S(k)]^2/(\kappa_{\text{tot}}^2 a^6)$. Dividing Eq. (C10) by this factor, we arrive at the shot noise suppression factor due to finite lifetimes:

$$f_{\text{FL}}(k, \mu) = \frac{1}{[S(k)]^2} \int_{-\infty}^{\infty} \frac{d\omega}{2\pi} \tilde{p}(\omega) \mathcal{H}\left(\frac{K}{a\kappa_{\text{tot}}}, \frac{\omega}{\kappa_{\text{tot}}c}\right). \quad (\text{C13})$$

In the case that the quasars are ‘‘on’’ for a duration of time t_Q , then the conditional probability of being on at a later time is a triangle function:

$$p(\Delta t) = \begin{cases} 1 - |\Delta t|/t_Q & |\Delta t| < t_Q \\ 0 & |\Delta t| \geq t_Q \end{cases}, \quad (\text{C14})$$

so

$$\tilde{p}(\omega) = t_Q \left[\frac{\sin(\omega t_Q/2)}{(\omega t_Q/2)} \right]^2. \quad (\text{C15})$$

We cannot find an analytic solution to the integral in Eq. (C13). However, it is a one-dimensional integral of elementary functions and thus easily solvable numerically. Results are shown in Fig. C2. We see that at large scales, there is a large suppression of the shot noise contribution to ionizing background fluctuations, especially for the shorter quasar lifetimes. For $k \ll a/(ct_Q)$, the suppression factor f_{FL} is proportional to t_Q , consistent with the findings in Meiksin & McQuinn (2019, §2.3). At smaller scales (larger k), $f_{\text{FL}} \rightarrow 1$ and the shot noise power is unaffected. There is a modest dependence on the orientation of the wave vector with respect to the line of sight. For radial modes (large μ), a ‘‘high- k ringing’’ is visible where the ionizing background power spectrum is actually enhanced for some modes. The peak of f_{FL} is at $k \approx 2\pi a/(ct_Q)$, where the radial comoving distance between photons that left the quasar when it turned on and reverberated off the IGM behind the quasar and the photons that left the quasar when it turned off and came directly toward the observer ($ct_Q/2a$) is a half-wavelength. This feature moves to higher k for shorter quasar lifetimes. The ringing makes sense given that the model assumed the same lifetime for all quasars, but would probably be smoothed out in a realistic scenario.

We see that the very large suppression factors f_{FL} are obtained at the lowest k , which we do not use in our analysis. At the largest scale we use, $k = 0.015h \text{ Mpc}^{-1}$ and $\mu = 1$, the suppression factors can still be significant – they are 0.085, 0.23, and 0.55 for quasar lifetimes of 10^7 , $10^{7.5}$, and 10^8 yr respectively. So for long quasar lifetimes (10^8 yr), there is only a modest reduction in the shot noise factor, whereas for the short lifetimes the shot noise could be very dramatically reduced.

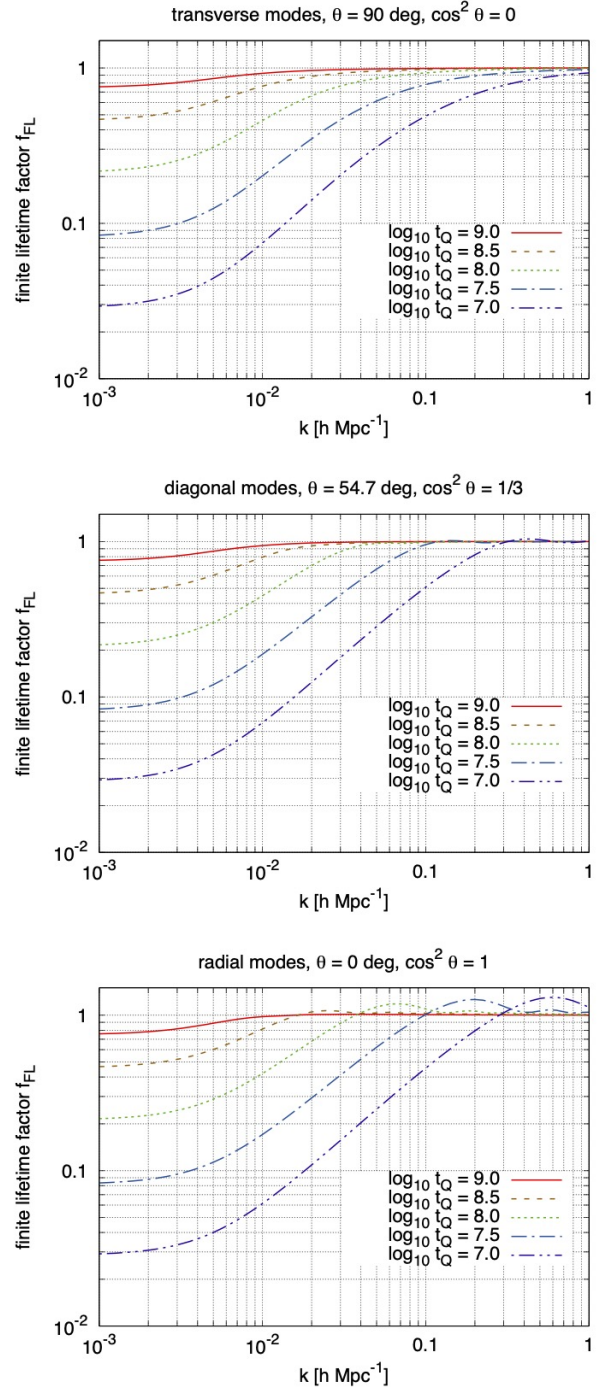


Figure C2. The factor f_{FL} by which shot noise in the ionizing radiation field is suppressed by finite quasar lifetimes, as given by Eq. (C13). The top panel shows transverse modes ($\mu = 0$); the middle panel shows diagonal modes at the root of the P_2 Legendre polynomial ($\mu = 1/\sqrt{3}$); and the bottom panel shows radial modes ($\mu = 1$). The five curves show quasar lifetimes ranging from $t_Q = 10^9$ yr (solid red, for illustration only since this is extremely long) through 10^7 yr (dot-dot-dashed purple).